

ON THE USE AND LIMITATIONS OF FLASH THERMOGRAPHY
TECHNIQUES FOR DETECTING DEFECTS IN VARIOUS METALLIC
MATERIALS

by

Kevin Patel

A thesis submitted to the faculty of
The University of North Carolina at Charlotte
in partial fulfillment of the requirements
for the degree of Master of Science in
Mechanical Engineering

Charlotte

2019

Approved by:

Dr. Harish P. Cherukuri

Dr. Christopher Evans

Dr. Angela Davies

ABSTRACT

KEVIN PATEL. On the use and Limitations of Flash Thermography Techniques for detecting Defects in Various Metallic Materials. (Under the direction of DR. HARISH P. CHERUKURI)

In this work, the predictive capabilities of Flash Thermography, a non-destructive testing method, in detecting the presence of defects in metallic parts are investigated using the Finite Element Method (FEM). Finite-element simulations of flash thermography on an artifact under inspection are carried out to understand the effect that various thermal and process parameters have on the temperature distribution in the artifact. The 1D analytical models for the finite and semi-infinite plate are studied to get an insight into the heat conduction process. Numerical models for finite width and semi-infinite plate are developed in ABAQUS Explicit, and the results are compared with the analytical model for validation. The thermal signal processing techniques, "Thermal Signal Reconstruction" (TSR) and "Coefficient Maps" (CM) are reviewed in this work to critique their extent of applicability for different process parameters.

TSR's dependability on the selection of the higher order polynomial and requirement of well-defined flash duration makes it unsuitable for in-situ measurement in an additive manufactured part. CM algorithm is tested on the numerical models having a flash duration longer than the diffusion time to signify the presence of the defect. Several numerical models are developed with different parameters for this study. Lastly, a qualitative comparison highlighting the unique features and the limitations of both the algorithm is presented.

DEDICATION

I dedicate my thesis to my parents, Kartika Patel and Atul Patel and my sisters, Dhruvi Patel and Nidhi Patel.

ACKNOWLEDGEMENTS

I want to express my sincere gratitude to my advisor Dr. Harish Cherukuri, for giving me this opportunity and guiding me through every aspect of this work. His continuous encouragement, guidance, support, and mentoring throughout the Research project helped me to get the best out of me.

I would like to extend my gratitude to Dr. Christopher Evans and Dr. Angela Davies for serving on my committee, and giving their valuable inputs, critical reviews and encouraging me to explore new ideas.

I am grateful to Dr. Bin Zhang for helping me get started with this project and providing with all the required materials.

I would like to thank my parents, family and friends for their moral support, encouragement and motivation throughout this endeavor of pursuing higher education, without which this would not have possible.

I would like to thank my friend Tilak Patel for giving his valuable feedback and critical reviews over the thesis.

Finally, I would like to thank all the members from my research group and the computational mechanics lab group for their help and support throughout this project.

TABLE OF CONTENTS

LIST OF TABLES	viii
LIST OF FIGURES	ix
LIST OF ABBREVIATIONS	xii
CHAPTER 1: INTRODUCTION	1
1.1. Thesis Objective	3
1.2. Thesis Outline	4
CHAPTER 2: LITERATURE REVIEW	5
2.1. Passive Thermography vs Active Thermography	5
2.2. Signal Processing Techniques	7
2.2.1. Thermal Contrast Technique	7
2.2.2. Pulsed Phase Thermography	8
2.2.3. Thermal Signal Reconstruction	9
2.3. Comparison Of PPT And TSR In Detecting Defects	10
2.4. Coefficient Map	10
2.5. Defect Detectability In Different Materials	11
CHAPTER 3: THERMOGRAPHIC SIGNAL RECONSTRUCTION METHOD	12
3.1. Background	12
3.2. FBH Defect In A SS-316l Block	12
3.3. A Circular Defect In A 2D Square Block	17
3.4. Three Defects Located At Varying Depth	20

CHAPTER 4: COEFFICIENT MAPS	23
4.1. Background	23
4.1.1. Analytical solution for semi-infinite and finite width plate for square pulse-heat source	23
4.1.2. Comparison of analytical and numerical solution for finite width plate	25
4.2. Boundary Conditions	26
4.3. Introduction Of Defect	28
4.4. Defect At Varying Depth	32
4.5. Multiple Defects In A Row	37
4.5.1. Modeling of two inline defects	37
4.5.2. Media with multiple defects at varying distance	39
4.5.3. Media with multiple defects at equidistance from each other	41
4.6. Detecting Defects In Different Materials	42
4.6.1. Defect detection in Ti64, Inconel and Copper	43
4.6.2. Defect detection in Copper	44
4.7. Comparison Based On The Depth Of The Material	45
4.8. Processing The Heating Curves For Copper	47
CHAPTER 5: CONCLUSIONS AND FUTURE WORK	50
5.1. Conclusions	50
5.2. Future Work	51
REFERENCES	52

LIST OF TABLES

TABLE 3.1: Thermal Properties of SS-316l [1]	13
TABLE 3.2: Quantification of defect depth for 4 th , 5 th , and 6 th order polynomial	20
TABLE 4.1: General boundary condition equation for 1D heat conduction problem	27
TABLE 4.2: Thermal Properties of Air [1]	29
TABLE 4.3: Material Properties of Ti64, Inconel and Copper [1]	43

LIST OF FIGURES

FIGURE 1.1: Schematics of Active Thermography.	2
FIGURE 2.1: The excitation signals for (a) pulse thermography (PT), (b) step thermography (ST), (c) lock-in thermography (LT) and (d) frequency modulation thermography (FMT)	6
FIGURE 3.1: (a) Top view, and (b) Bottom view, of a FBH defect in SS-316l with remaining wall thickness of 0.5 mm.	13
FIGURE 3.2: (a) Comparison of temporal variation of temperature for a node on the surface which is away from the defect and for a node on the defect. (b) Plot of change in temperature with respect to time(frames) for the same nodes.	14
FIGURE 3.3: (a) Logarithmic scale of the cooling curve. (b) Skipping post flash data in the logarithmic scale to avoid non-linearity during the curve fit.	15
FIGURE 3.4: 4 th order polynomial curve fit (a) First derivative plot. (b) Second derivative plot. 5 th order polynomial curve fit (c) First derivative plot. (d) Second derivative plot.	16
FIGURE 3.5: Defect located 100 μm from the top surface.	17
FIGURE 3.6: (a) Comparison of temporal variation of temperature for a node on the surface which is away from the defect and for a node on the defect. (b) Plot of change in temperature w.r.t time(frames) for the same nodes. (c) Logarithmic scale.	18
FIGURE 3.7: 2 nd derivative of (a) 4 th order polynomial. (b) 5 th order polynomial. (c) 6 th order polynomial. (d) Depth of the defect for different polynomial orders and post-flash frames.	19
FIGURE 3.8: Defect located 100 μm , 150 μm , 200 μm from the top surface from left to right.	21
FIGURE 3.9: (a) Comparison of temporal variation of temperature for four nodes on the surface. (b) Plot of change in temperature w.r.t time(frames) for those same nodes. (c) Logarithmic scale. (d) Logarithmic plot after skipping post flash frames.	21

FIGURE 3.10: (a) 1 st derivative plot of 8 th order polynomial. (b) 2 nd derivative plot of 8 th order polynomial.	22
FIGURE 4.1: Comparison of Semi-infinite and finite plate thickness.	24
FIGURE 4.2: Square pulse heat flux.	25
FIGURE 4.3: Exact and Numerical solution.	26
FIGURE 4.4: FEA model for defect free sample.	27
FIGURE 4.5: Effect of boundary condition on temperature distribution.	28
FIGURE 4.6: Air inclusion in the SS-316l block.	28
FIGURE 4.7: (a) Temporal variation of temperature for two nodes. (b) Logarithmic scale of change in temperature w.r.t frames.	30
FIGURE 4.8: (a) <i>c</i> -map (b) <i>b</i> -map. (c) Plot of slope vs x-position. (d) Plot of intercept vs x-position.	31
FIGURE 4.9: Temporal variation of temperature for a defect located at (a) 10 μm deep. (b) 25 μm deep. (c) 50 μm deep. (d) 100 μm deep.	32
FIGURE 4.10: Logarithmic scale of temperature profile for a defect located at (a) 10 μm deep. (b) 25 μm deep. (c) 50 μm deep. (d) 100 μm deep.	33
FIGURE 4.11: <i>c</i> -maps and magnitude of slope w.r.t position for a defect located at (a), (b) 10 μm deep. (c), (d) 25 μm deep. (e), (f) 50 μm deep. (g), (h) 100 μm deep.	35
FIGURE 4.12: <i>b</i> -maps and magnitude of intercept w.r.t position for a defect located at (a), (b) 10 μm deep. (c), (d) 25 μm deep. (e), (f) 50 μm deep. (g), (h) 100 μm deep.	36
FIGURE 4.13: Schematics of two defects placed together at 50 μm beneath the top surface in SS-316l block.	37
FIGURE 4.14: (a) <i>c</i> -map for two inline defects. (b) Magnitude of slope w.r.t. x-position. (c) <i>b</i> -map for two inline defects. (d) Magnitude of intercept w.r.t x-position	38

FIGURE 4.15: (a) Schematics of multiple defects placed together at 10 μm beneath the top surface. (b) Sectional view.	39
FIGURE 4.16: (a) c -map for multiple defects. (b) Magnitude of slope w.r.t. x -position. (c) b -map for multiple defects. (d) Magnitude of intercept w.r.t x -position.	40
FIGURE 4.17: Schematics of multiple defects placed equidistant from each other, at 10 μm beneath the top surface.	41
FIGURE 4.18: (a) c -map for multiple defects equidistant from each other. (b) Magnitude of slope w.r.t. x -position. (c) b -map for multiple defects equidistant from each other. (d) Magnitude of intercept w.r.t x -position.	42
FIGURE 4.19: Comparison of thermograms of Ti-64 and Inconel (a) Defect-free node. (b) Node over the defect.	44
FIGURE 4.20: Comparison of thermograms of Ti-64 and Inconel (a) Defect-free node. (b) Node over the defect.	44
FIGURE 4.21: Temperature distribution of defect and defect-free node for copper.	45
FIGURE 4.22: (a) Spatial variation of slope for 10 μm deep defect. (b) Spatial variation of intercept for 10 μm deep defect.	46
FIGURE 4.23: (a) Spatial variation of slope for 50 μm deep defect. (b) Spatial variation of intercept for 50 μm deep defect.	46
FIGURE 4.24: (a) Spatial variation of slope for 100 μm deep defect. (b) Spatial variation of intercept for 100 μm deep defect.	47
FIGURE 4.25: (a) Temporal variation of temperature for a 10 μm deep defect in copper. (b) Change in temperature transformed to logarithmic scale.	48
FIGURE 4.26: For 50 μm deep defect in copper (a) c -map. (b) magnitude of slope. For 100 μm deep defect in copper (c) c -map. (d) magnitude of slope.	49

LIST OF ABBREVIATIONS

AM	Additive Manufacturing
BJ	Binder Jetting
CM	Coefficient Maps
CT	Computed Tomography
DLP	Digital Light Processing
FBH	Flat Bottom Hole
FDM	Fused deposition Modeling
FEM	Finite Element Method
FMT	Frequency Modulated Thermography
FT	Flash Thermography
IR	Infrared
LT	Lock-in Thermography
NDT	Non-destructive test
PPT	Pulsed Phase Transform
PT	Pulse Thermography
SLA	Stereolithography
SLM	Selective Laser Melting
SLS	Selective Laser Sintering
ST	Step Thermography

TSR Thermal Signal Reconstruction

UT Ultrasonic Test

CHAPTER 1: INTRODUCTION

Additive Manufacturing (AM) is gaining attention because of its rapid prototyping ability, the ability to manufacture intricate geometries, flexibility in changing the design, and controlling the material properties. These capabilities give it an edge over the subtractive manufacturing which is time consuming and requires special tools and fixtures to manufacture a part [2]. Subtractive manufacturing removes the material to obtain the desired shape, which causes higher material waste. AM on the other hand, add the layers of the material on the specific locations thereby reducing the material waste. The inferior surface finishing of an AM part is improved by utilizing post-processing techniques such as grinding, polishing, chemical post-processing treatments and CNC Finishing/Machining [3]. Industries such as aerospace, automotive, medical, machinery and defense have adopted AM to increase the production and cut the lead time for fabrication. There are several 3D printing techniques such as Stereolithography (SLA), Digital Light Processing (DLP), Fused Deposition Modeling (FDM), Selective Laser Sintering (SLS), Selective Laser Melting (SLM), Binder Jetting (BJ) [4]. Depending on the application, the AM technique is selected.

Although AM is an alternative to the conventional manufacturing processes. However, it has certain drawbacks namely dimensional accuracy, finishing and the size of the part that gets printed on the test bed. With metal AM, dimensional accuracy, surface finish and unfused powder particles are of significant concern since it directly affects the mechanical properties and the life span of the part. The scanning speed of the laser and incorrect laser power are some process parameters that impact the origination of these defects. Application areas such as aerospace, spaceships, automobiles, pressure vessel, turbines, have demanding mechanical specifications where

a minute defect could lead to catastrophic consequences. Due to incorrect process parameters in 3D manufacturing, sometimes the powder fails to melt leaving pores or cracks in that layer, and these minor flaws are responsible for the failure of the part. Hence, there is a need for an in-situ method to sense defects as they occur.

The visible surface flaws can be easily tracked down with simple visual inspection. However, to find the subsurface defects either destructive testing or non-destructive testing needs to be conducted on the specimen. Destructive testing involves tests like tensile or compression test which deforms the sample, and it is expensive. Non-destructive tests (NDT) such as X-ray Computed Tomography (CT), Ultrasonic Test (UT), Dye-penetration and Flash Thermography (FT) do not cause damage to the part. A Dye-penetration test can only detect flaws on the top surface [5]. X-ray CT and UT tests can penetrate the surface, but these tests are time-consuming and expensive [5]. FT is another alternative to detect internal anomalies without having any contact between the work-piece and the apparatus. It is also quicker and cheaper compared to X-ray CT and UT.

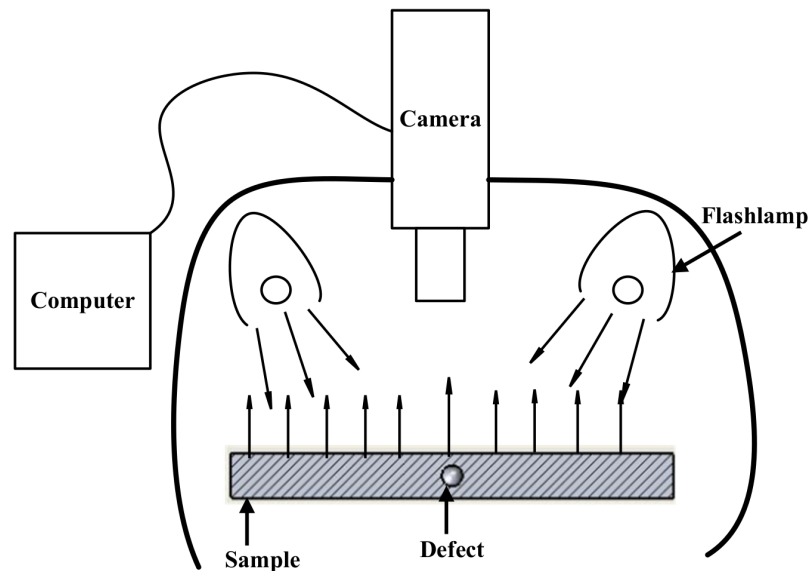


Figure 1.1: Schematics of Active Thermography

Figure 1.1 shows the working principle of active thermography where an external source (flash lamps) heats the surface of the sample, and the infrared (IR) camera captures an image of the IR radiation leaving the surface of the sample. The applied heat diffuses into the material, but defects in the sample impact the heat diffusion thereby causing a temperature variation, and therefore IR radiation differences on the top surface. The IR camera takes several images of the sample's surface and records the variation in the emission of the IR radiation. An algorithm converts the image data to a temperature vs. time profile, which is used to signify the presence of the defect. The real challenge is to use the available temperature data and quantify the depth, size, and shape of the defect. There has been a significant amount of work done in this field in the past 2 decades where new signal processing techniques such as 'Pulsed Phase Transform' (PPT), 'Thermal contrast method' and 'Thermal Signal Reconstruction' (TSR) [6] have been developed.

1.1 Thesis Objective

The objectives of the present study are the following:

- Investigate the ability of the TSR to predict the depth of the defect for defects close to the top surface.
- Study the analytical model of the defect-free plate with an instantaneous heat source.
- Correlate the 1D analytical and numerical model of the finite width plate subjected to the surface heat flux of duration τ for validation of numerical results.
- Analyze a new signal processing technique called coefficient maps (CM)[7].
- Conduct a parametric study on CM to test its applicability.

1.2 Thesis Outline

Chapter 1 gives a brief introduction about AM, and its application in various industries. It describes the problem statement and the objective of this thesis. During 3D printing, defects can occur within a few layers of the part surface. Hence, there is a need for a cost-effective technique to characterize those defects without any damage to the work-piece.

Chapter 2 discuss the active and passive thermography followed by different signal processing techniques used in analyzing defect localization. In addition, a comparison of the two most popular signal processing techniques will be conducted. This is followed by a detectability test to identify defects in different materials.

Chapter 3 focuses on the modeling and analysis of the TSR technique to predict the depth of the defect. It also points out the shortcomings of the TSR technique, thereby indicating the need for a new signal processing technique.

Chapter 4 is about studying the analytical solutions for semi-infinite and finite width plate to understand the heat transfer phenomenon. The numerical model for the finite width plate is validated by comparing the numerical result with the analytical solution for the square pulse heat source. The new signal processing technique CM proposed by B. Zhang et al. is applied on the numerical results obtained from the ABAQUS to signify the presence of the defect. The numerical models are developed for the flash duration longer than the diffusion time. The temporal variation of the temperature is recorded in the ABAQUS and further processed in the MATLAB by using the CM signal processing algorithm. A parametric study is conducted to test its applicability and limitations.

Lastly, in Chapter 5, the conclusions are made based on the results obtained by comparing both techniques. Future work is presented to extend the scope of the presented work.

CHAPTER 2: LITERATURE REVIEW

Above absolute zero temperature (0 °K) all objects emit IR radiations which can be captured using IR camera. The IR camera captures the radiation and convert it to an electronic signal which can be further utilized to generate thermal images. These thermal images have a higher temperature region or a hot-spot in some areas, which signify the presence of a void defect beneath that location and a relatively lower temperature over the areas without a defect. This process of identifying surface or sub-surface abnormalities without making any contact with the sample is called thermography [8]. It is classified mainly in two categories active thermography and passive thermography which differ based on the excitation used to create the temperature gradient of the system from the surrounding.

2.1 Passive Thermography vs Active Thermography

In passive thermography, the specimen of interest is at a higher temperature than its surrounding; hence it does not require any heat source to raise the temperature. Passive thermography can be conducted on buildings and the human body because they have a temperature gradient w.r.t the surrounding. However, the absence of thermal stimulus gives less contrast on the surface, and due to this, the defects far from the surface might remain unnoticed.

In the case of active thermography, the sample is heated using an external heat source to create a difference in the temperature of the sample from the ambient. It can be used to identify the defects that are far from the surface. Pulsed thermography (PT), pulsed phase thermography [9, 10], lock-in thermography (LT) [11], step thermography (ST) [12], and frequency modulated thermography (FMT) [13, 14] are

different forms of excitation signals that fall under active thermography.

Figure 2.1 (a) shows the PT wherein a pulse of energy is applied for a short time, increasing the surface temperature, and the sample is allowed to cool. The measurements (temporal variation of surface temperature) are taken while the sample is cooling. This type of excitation is also called flash heating. In ST, as shown in figure 2.1 (b), constant energy of lower flux is continuously supplied to the specimen, and the measurements are taken during the application of the energy. Figure 2.1 (c) shows a periodic excitation utilized to extract phase information from the reflected thermal wave. This sort of phase extraction using periodic excitation is called LT. FMT is slightly different than LT. It is used when phases are to be extracted from a large number of thermal waves having distinct frequencies.

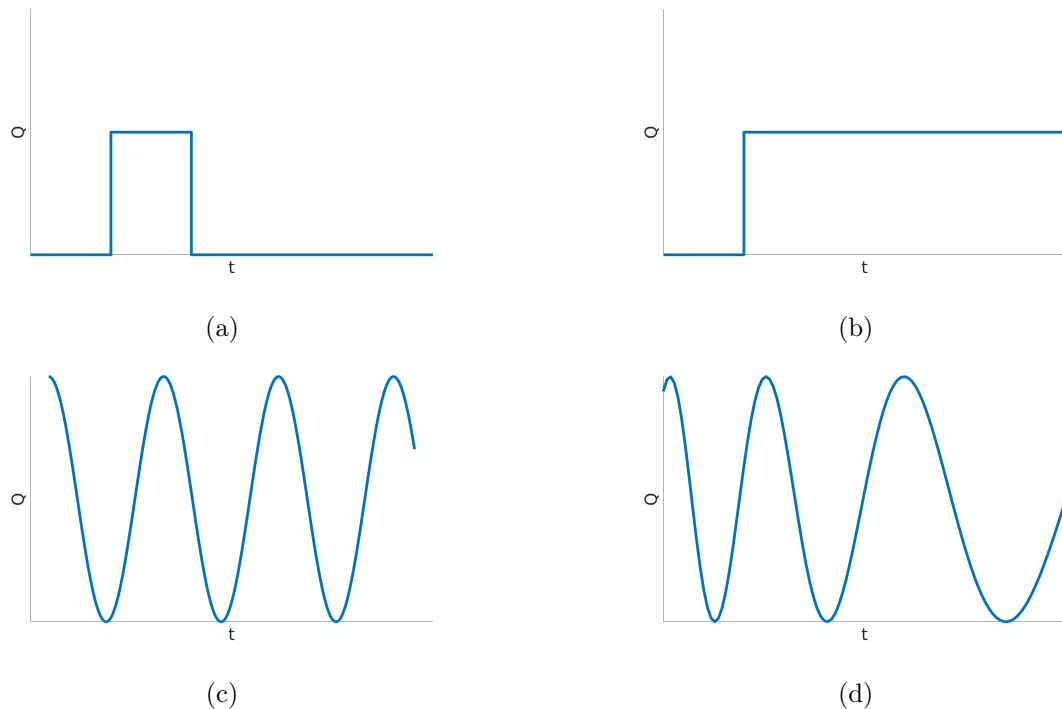


Figure 2.1: The excitation signals for (a) pulse thermography (PT), (b) step thermography (ST), (c) lock-in thermography (LT) and (d) frequency modulation thermography (FMT)

Active thermography has an advantage over passive thermography to detect deeper

sub-surface defects, delaminations, voids, and inclusions because of the presence of the heat source which increases the temperature gradient. As a result, the thermograms obtained by the IR camera have better signal to noise ratio. Also, compared to all the available excitation sources, flash thermography is the cheapest means to conduct NDT because it is easy to use and quick to raise the temperature of the specimen [15]. ST can detect a more profound defect, but it can have an adverse effect on the temperature measurement because of the continuous heating. LT has an advantage over PT in quantifying subsurface defects, but for identifying various defects in the same part, the experiments have to be repeated along with changing the frequency of the thermal wave which makes it time-consuming. FMT is very sensitive for estimating the location of a discontinuity and it is independent of the emissivity of the material, but the system is extremely complex compared to PT. Flash heating can be utilized for detecting the defects by implementing a better signal processing technique.

2.2 Signal Processing Techniques

The traditional way to characterize a discontinuity is by heating the surface and capturing its cooling behavior through an IR camera. The captured images will visually show a localized hot-spot indicating the presence of the defect [16]. Visual inspection alone is highly subjective, and can be incorrect with complex geometries. Attempts have been made to manipulate the thermogram obtained from the IR camera to extract valuable information like the presence of the sub-surface defect and predicting the depth of the defect [9, 17, 18]. Numerous techniques have been developed to predict the presence of the defect.

2.2.1 Thermal Contrast Technique

This signal processing technique compares the change in temperature of the pixel over the defect region with the reference pixel to compute the contrast. The reference

pixel needs to be on a defect-free region [17]. In the case of a non-uniform heat distribution, the pixels on the defect-free region have a different temperature distribution thereby causing a conflict in choosing a pixel to be compared with the pixel over the defect. Thus, selection of the defect-free pixel is always a challenge, and the result varies based on the reference pixel. The absolute thermal contrast ($\Delta T(t)$) is given by the following expression [17]:

$$\Delta T(t) = T_d(t) - T_{S_a}(t) \quad (2.1)$$

$\Delta T(t)$ is the difference between the temperature over the defect $T_d(t)$ and the sound region $T_{S_a}(t)$. Thus, the absolute thermal contrast technique requires the presence of a non-defective region in the field of view to bring out the defect in that particular region. Furthermore, if the defect is as significant as the field of view, there will not be any reference pixel and hence, no contrast after processing the data. The part will be considered defect-free in the absence of the contrast which will be misleading [16].

2.2.2 Pulsed Phase Thermography

PPT involves computing the phase change of a thermal wave by performing a Fourier transform on the temperature decay of each pixel on the top surface [9]. The Fourier transform is calculated using the following equation:

$$F(u) = \frac{1}{N} \sum_{n=0}^{N-1} T(t) e^{\left(\frac{-j2\pi ut}{N} \right)} = R(u) + jI(u) \quad (2.2)$$

The real $R(u)$ and the imaginary $I(u)$ (u being the frequency variable) are used to compute the phase of the reflected thermal wave using

$$\phi(u) = \tan^{-1} \left(\frac{I(u)}{R(u)} \right) \quad (2.3)$$

The phase of the non-defective region is different from the defective region and thereby indicating contrast in the phase contrast map. The contrast indicates the presence of the defect in the specimen. The main advantage of PPT over the thermal contrast technique is that it does not require a reference (non-defective) region to carry out the

signal processing and it has a better resolution than the thermal contrast technique.

2.2.3 Thermal Signal Reconstruction

TSR is considered a novelty in the field of FT because it is based on the 1D analytical heat conduction in a semi-infinite medium with a Dirac heat pulse [18]. The governing differential equation for heat conduction is given by

$$\frac{\partial^2 T}{\partial z^2} - \frac{1}{\alpha} \frac{\partial T}{\partial t} = 0 \quad (2.4)$$

where α is the diffusivity of the material which is given by $\alpha = \frac{\kappa}{\rho c}$ (m^2/s). The solution of this differential equation for the insulated boundary condition is given by

$$\Delta T = \frac{Q}{e\sqrt{\pi t}} \quad (2.5)$$

where Q is the energy imparted on the surface (J/m^2), e is the effusivity ($e = \sqrt{\kappa c \rho}$) ($\text{J}/\sqrt{\text{s}}\text{m}^2\text{K}$) and t is the time taken by the heat front to reach the back wall of the specimen [18, 19]. The logarithmic form of the above equation is

$$\ln(\Delta T) = \ln\left(\frac{Q}{e}\right) - \frac{1}{2} \ln(\pi t) \quad (2.6)$$

Thus, the temperature decreases with the square root of time t . For a 1D heat transfer problem, the slope will be -0.5. Any deviation from this value represents the presence of discontinuities in the material. It is known that heat diffuses in all three directions, but for a defect-free component, the lateral components will cancel out. Based on this model, the interest is in finding the time at which the 1D heat diffusion ends or the time instance when the slope of the cooling curve diverges from -0.5 to locate the depth of the defect. The depth of the defect is calculated using the expression given below [20]

$$t = \frac{L^2}{\pi\alpha} \quad (2.7)$$

The cooling curve of a pixel is converted to a logarithmic scale to linearize the data. A polynomial of order 'n' is used to approximate the log scale. This curve fitting tool is called a low pass filter. Since heat conduction is the low-frequency problem, any

high-frequency content in the data is noise, and the curve fitting will eliminate the noise thereby increasing the signal to noise ratio [16]. This n^{th} order polynomial is differentiated twice. The peak in the second derivative will give the time at which the heat front reaches the back wall of the part (if the part is defect-free). If there is a defect in a part, the first peak will occur at an earlier time that corresponds to the time at which the heat front reaches the defect. This method can also be used to find the material properties.

2.3 Comparison Of PPT And TSR In Detecting Defects

B. Oswald-Tranta, R.Schmidt, T.Grandl, 2016 compared two thermal signal processing techniques, PPT, and TSR on a flat bottom hole (FBH) defect and material inclusions in bulk to see if they can characterize the defect using either technique [21]. They used FEA to model the defect in a sample as well as conducted FT experiments on a 3D manufactured plastic with an air inclusion and an aluminum inclusion as a defect. After processing the finite element results and the experimental results, it was concluded that the PPT and TSR techniques give almost the same result for flat bottom hole defect and air inclusion.

2.4 Coefficient Map

TSR approach fails to account for near surface defects because it assumes that the diffusion length is large enough and the lateral heat diffusion begins when the specimen is cooling [7]. In the case of additive manufacturing, it is possible that the defect is 10's of microns from the top layer and if the diffusion time is less than the flash duration, the defect will go unnoticed and the second derivative peak will not give the correct depth of the defect. The coefficient map approach allows for this and provides a way to process thermograms even for a flash time longer than the diffusion time.

2.5 Defect Detectability In Different Materials

Heat conduction in a material highly depends on the thermal conductivity κ (W/mK) because the higher the conductivity, the more rapidly heat will conduct through the material. To capture a defect in a highly conductive material, a camera with a higher frame rate is required. Maierhofer et al., 2016 conducted a round robin test on FT to test the detectability of defects of various size in different materials. Nine participants took part in this experiment to carry out FT on steel, aluminum, copper and carbon fiber reinforced polymer. Among all the materials, copper had the highest conductivity, which resulted in copper heating quickly through the bulk. Large flat bottom holes (FBH) were captured by a few high-spec IR cameras but no signature of small FBH near the surface [22].

From the literature, it is clear that the CM method is sensitive to near surface defects and longer flash duration which the TSR is not. Also, for materials with higher thermal conductivity, the cooling curve might not show any signs of defect, hence the 2nd derivative peak will not correspond to the diffusion time. There is a need to investigate both the signal processing techniques further to find the maximum depth at which a signature of the defect can be seen on the top surface and also consider different materials to study the effect of their properties on the heat diffusion. It is quite expensive to conduct FT on different materials and with defects located at varying depth. A better approach is to conduct FEA and model FT in a finite element package to get the spatial and temporal variation of the temperature and post-process them in MATLAB to signify the presence of the defect.

CHAPTER 3: THERMOGRAPHIC SIGNAL RECONSTRUCTION METHOD

3.1 Background

The 1D analytical model is the base for the TSR technique as described in the previous section but that analytical model is derived using the Dirac delta function for the flash duration. In reality, this is not the case. In TSR, the diffusion length is assumed to be sufficiently large enough that the heat diffusion behaves purely as a 1D model. The heat diffusion is affected while the flash is turned off and the sample is cooling. The heat starts to accumulate over the defect, and the diffusion process slows down near the vicinity of the defect. At a distance significantly far from the defect, the diffusion process still behaves as 1D heat diffusion. Depending on the thermal conductivity of the defect compared to the parent material, the heat propagation will either accelerate or decelerate.

In TSR, the thermograms obtained from the IR camera are converted to a log scale to amplify the signal. After skipping the post-flash data, a polynomial of higher order is fitted on the log scale. The peak of the second derivative of that polynomial gives the diffusion time which can be used to estimate the depth of the defect. It is unclear which higher order polynomial to use to approximate the logarithmic curve. A finite element study is conducted to find which order polynomial suits best.

3.2 FBH Defect In A SS-316l Block

An SS-316l block ($20 \text{ mm} \times 20 \text{ mm} \times 1 \text{ mm}$) as shown in figure 3.1 below has a FBH defect with defect-free surface of 0.5 mm thickness. The magnitude of the heat flux is 10 MW/m^2 , applied for 2.5 ms at the top surface, and the simulation runs for 50 ms with a $10 \text{ }\mu\text{s}$ time increment. The flash duration is selected after calculating

the diffusion time using Equation (2.7) to make sure that the diffusion time is larger than the flash duration. The initial temperature of the block is taken to be room temperature, i.e., 20°C (293 K) and the boundaries are insulated. The thermal properties of the SS-316l used in the simulation are shown in Table 3.1.

Table 3.1: Thermal Properties of SS-316l [1]

Material Properties	Thermal Conductivity κ (W/mK)	Density ρ (kg/m ³)	Specific Heat Capacity C_p (J/kgK)	Diffusivity $\alpha = \frac{\kappa}{\rho C_p}$ (m ² /s)
SS-316l	15	7970	510	3.7e-6

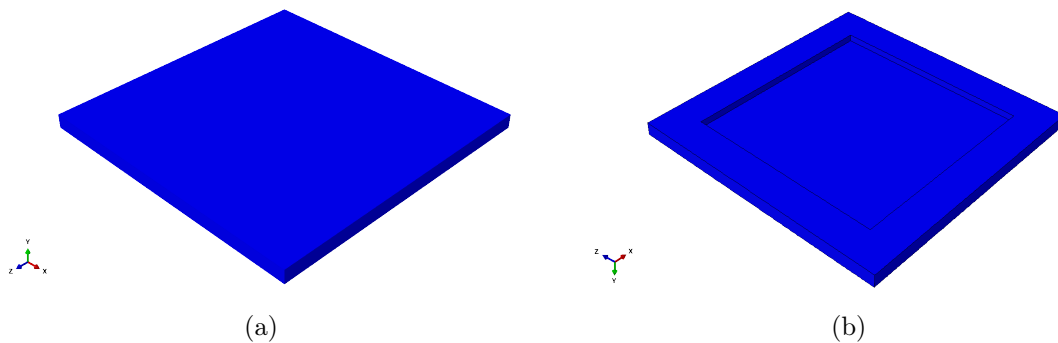


Figure 3.1: (a) Top view, and (b) Bottom view, of a FBH defect in SS-316l with remaining wall thickness of 0.5 mm.

The specimen exhibits simple 1D heat diffusion until 0.5 mm deep the heat flux reaches in the block for all the nodes, so the temperature vs. time profile for all the nodes are the same until 21 ms (obtained using Equation (2.7)). There is heat accumulation as a result of the FBH, and hence, the cooling rate is different for the nodes over the FBH than the nodes over the defect-free region. The nodes over the defect cool down at a slower rate than the nodes over the defect-free region. Figure 3.2 (a) shows the thermograms of two nodes, one node is over the FBH and the second is over the defect-free region. The temporal variation of the temperature for both the

nodes is the same until 21 ms. Thereafter, they diverge due to the heat accumulating over the FBH. Figure 3.2 (b) shows the plot of change in temperature versus time frames. The main reason for converting the time to the frames is because the images obtained from the IR camera are in terms of frames. This conversion does not have any effect in further calculations.

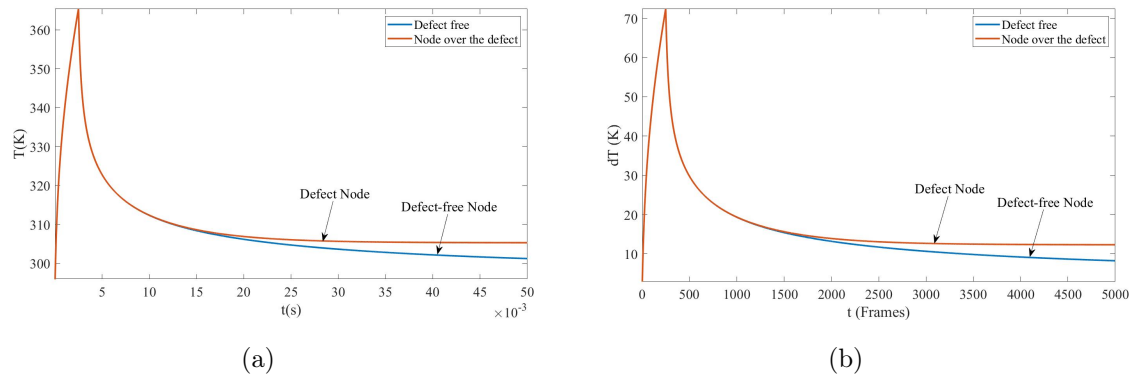


Figure 3.2: (a) Comparison of temporal variation of temperature for a node on the surface which is away from the defect and for a node on the defect. (b) Plot of change in temperature with respect to time(frames) for the same nodes.

The moment at which the heat flux or the energy source is turned off, there is a sharp drop in the temperature causing non-linearity at the beginning of the cooling curve [16]. Therefore the cooling curves are transformed to the logarithmic scale to linearize the data and amplify the signal as shown in figure 3.3 (a). The first few frames are skipped after turning off the heat source to avoid the non-linearity in calculating polynomials as shown in Figure 3.3 (b). The post-flash data in the curve fitting gives a poor fit because of the non-linearity in the logarithmic scale.

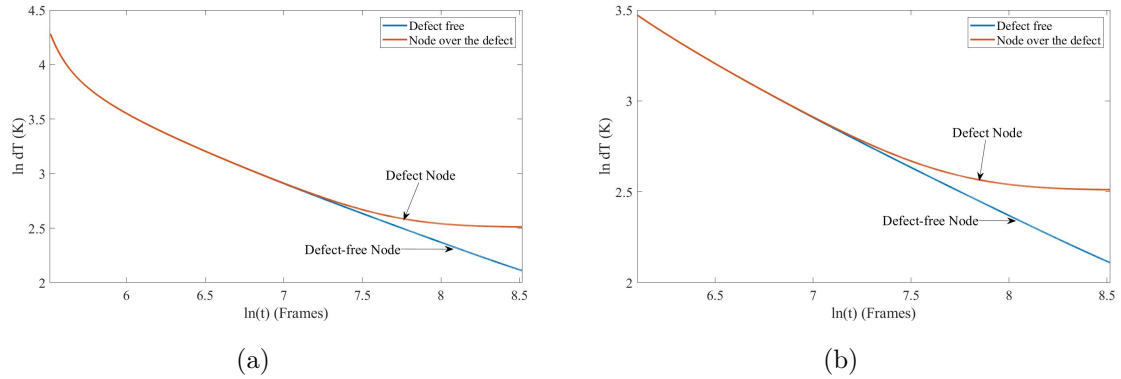


Figure 3.3: (a) Logarithmic scale of the cooling curve. (b) Skipping post flash data in the logarithmic scale to avoid non-linearity during the curve fit.

A polynomial of order 4th, 5th or 6th is fitted on the logarithmic scale to approximate the curves. Lastly, the polynomial is differentiated twice to quantify the depth of the defect. Here, the log scales are approximated using 4th and 5th order polynomial. Figure 3.4 (a) and (b) shows the first and second derivative for 4th order polynomial and figure 3.4 (c) and (d) shows the first and second derivative for 5th order polynomial. This study shows that the results highly depends upon the choice of the curve fitting polynomial order. The peak in the second derivative plot in Figure 3.4 (b) occurs at $\ln t = 7.7$ which corresponds to a 0.5 mm diffusion length, but with a 5th order polynomial fit, the peak occurs at the earlier time $\ln t = 7.8$ and the defect depth comes out to be 0.53 mm which gives false indication of the diffusion length.

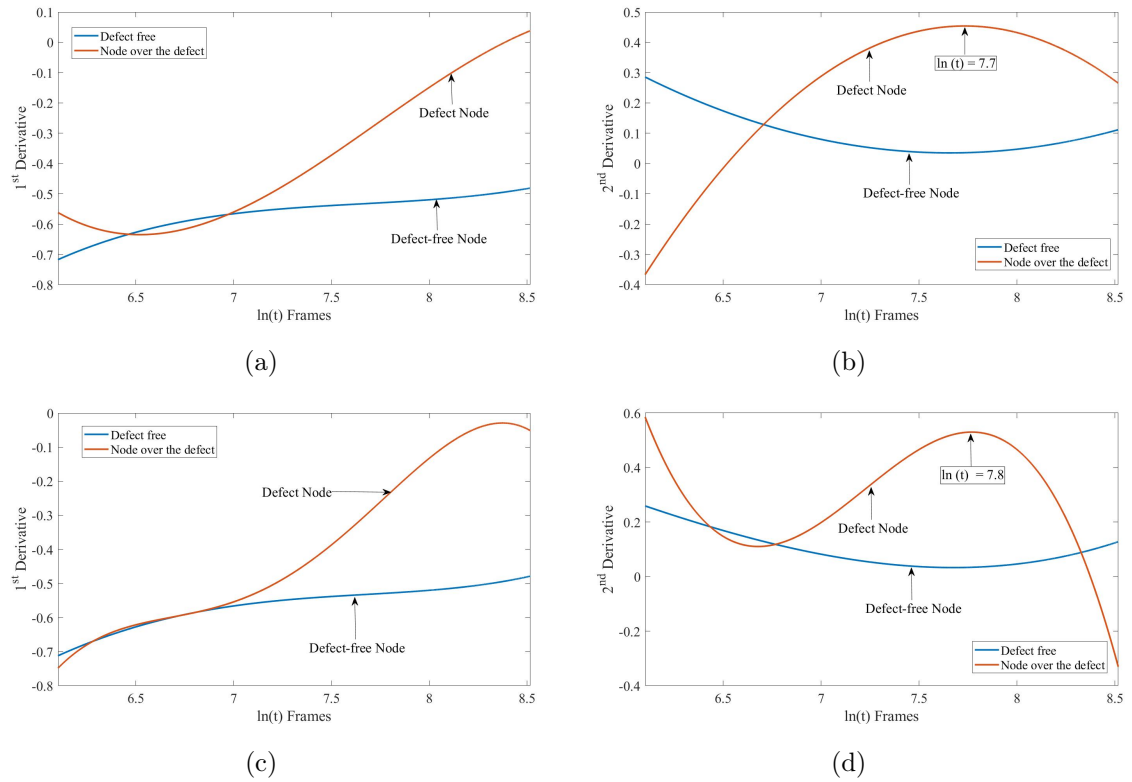


Figure 3.4: 4th order polynomial curve fit (a) First derivative plot. (b) Second derivative plot. 5th order polynomial curve fit (c) First derivative plot. (d) Second derivative plot.

3.3 A Circular Defect In A 2D Square Block

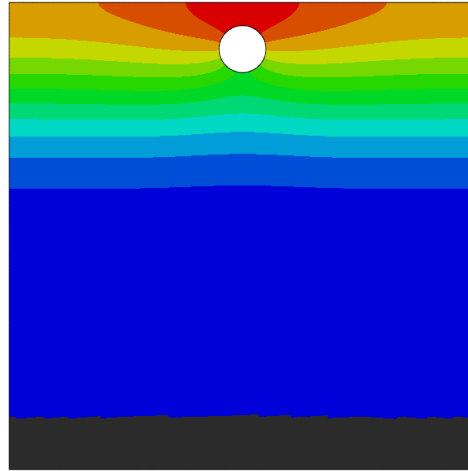


Figure 3.5: Defect located $100\ \mu\text{m}$ from the top surface.

A 2D square block of SS-316l of dimensions ($2\ \text{mm} \times 2\ \text{mm}$) with a circular hole of $200\ \mu\text{m}$ diameter located at a distance of $100\ \mu\text{m}$ from the top surface is shown in Figure 3.5. For this model, the heat flux is applied at the top with $1\ \text{MW}/\text{m}^2$ magnitude for $0.2\ \text{ms}$. The time duration of the heat is $5\ \text{ms}$ with the time step of $1\ \mu\text{s}$. The thermograms of the node over the defect and the node over the defect-free region on the top surface obtained are shown in Figure 3.6 (a) below, and the change in temperature vs frames is shown in Figure 3.6 (b). The same kind of trend follows here, wherein the flash duration is kept smaller than the characteristic-time for the heat flux to reach the defect. This results in a simple 1D heat diffusion until the heat flux reaches the defect. Deviation from 1D heat diffusion is only observed in the cooling curves. Figure 3.6 (c) is the logarithmic scale of the change in temperature and frames.

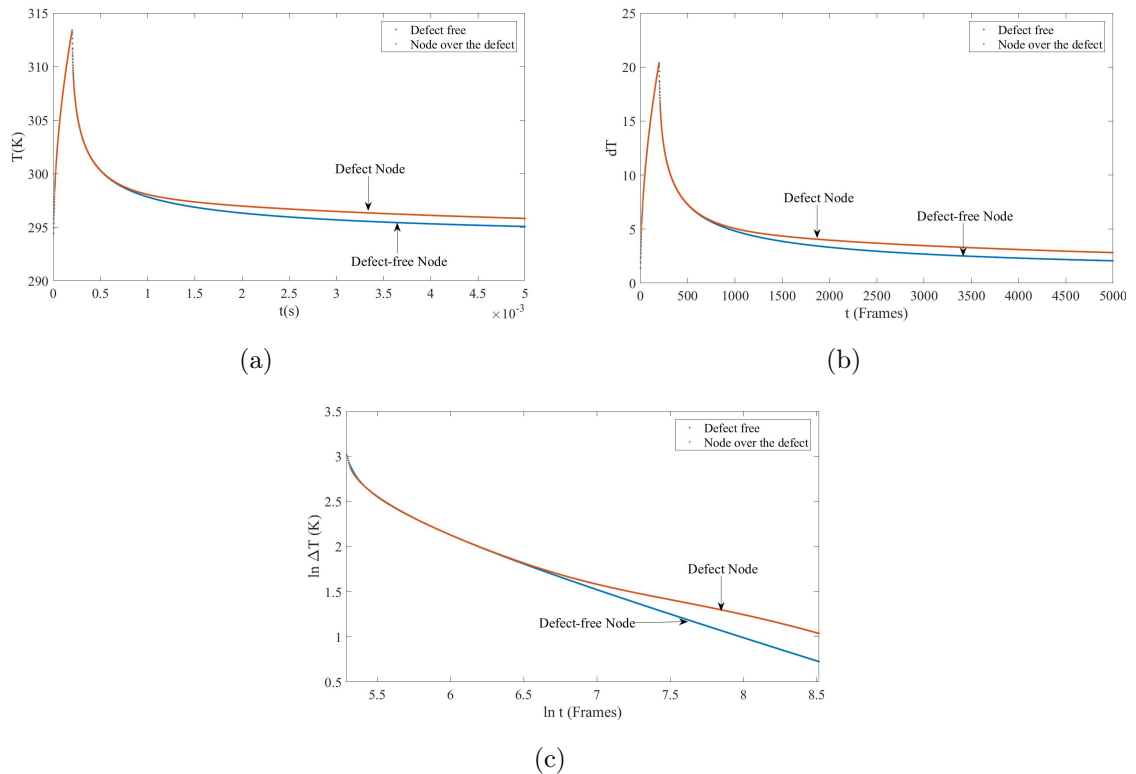


Figure 3.6: (a) Comparison of temporal variation of temperature for a node on the surface which is away from the defect and for a node on the defect. (b) Plot of change in temperature w.r.t time(frames) for the same nodes. (c) Logarithmic scale.

The curve fit on the log scale using 4th, 5th and 6th order polynomial is shown in the Figure 3.7 (a), (b) and (c), respectively. Also, each order of the polynomial is approximated after skipping a different number of post-flash frames. For this study, the post-flash frames taken under consideration are 20, 100, 300, 325, 350, 400 and 500. The curve fitting polynomial obtained after skipping the post-flash frames are then differentiated twice to get the diffusion length that corresponds to the depth of the defect. It is clear from the second derivative plots shown in Figure 3.7 that the selection of the post-flash frames is highly critical in estimating the defect's depth.

Since there is a non-linearity at the beginning of the cooling curve, skipping 20 frames, does not make a difference because the time increment is incredibly small here. For the higher order polynomials, the non-linearity needs to be avoided in

the curve fitting. Figure 3.7 (a) shows that the second derivative of the 4th order polynomial has a peak in the beginning. The corresponding depth obtained is shown in Figure 3.7 (d). For 4th order polynomial the second derivative peak fails to predict correct depth of the defect even after skipping 500 frames. The 5th order polynomial does succeed in giving a reasonably close prediction but only for a specified number of skipped post-flash frames. The 6th order polynomial provides the closest estimate to the actual depth of the defect. Table 3.2 quantifies the defect depth for each higher order polynomial using equation (2.7).

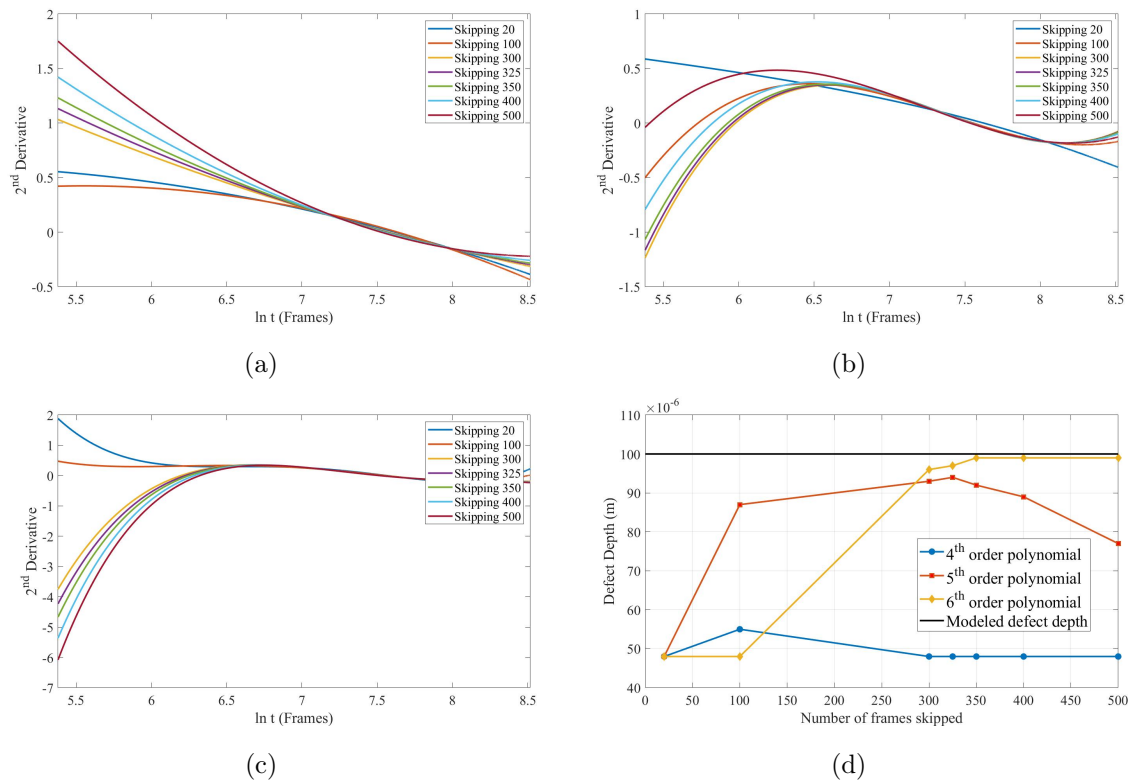


Figure 3.7: 2nd derivative of (a) 4th order polynomial. (b) 5th order polynomial. (c) 6th order polynomial. (d) Depth of the defect for different polynomial orders and post-flash frames.

This study shows that the order of the polynomial plays a vital role in assessing the defect location. The selection of the wrong polynomial gives an incorrect estimate of the defect. Also, the number of post-flash frames to be skipped is crucial as that

affects the coefficients in the polynomial.

Table 3.2: Quantification of defect depth for 4th, 5th, and 6th order polynomial

Post-flash frames skipped	4 th order polynomial	5 th order polynomial	6 th order polynomial
20	48 μm	48 μm	48 μm
100	55 μm	87 μm	48 μm
300	48 μm	93 μm	96 μm
325	48 μm	94 μm	97 μm
350	48 μm	92 μm	99 μm
400	48 μm	89 μm	99 μm
500	48 μm	77 μm	99 μm

3.4 Three Defects Located At Varying Depth

When there is more than one defect in a sample, the selection of the higher order polynomial needs to be done in such a way that it gives consistent result irrespective of the defect location. This study shows that the peak of the second derivative changes with the selection of the curve fitting parameters. Figure 3.8 shows a square block of dimensions (2 mm \times 2 mm) with a circular hole of a diameter of 200 μm located at a distance of 100 μm , 150 μm , and 200 μm (from left to right) from the top surface. This study aims to find the best suitable curve fitting parameter that gives consistent results for each defect. Figure 3.9 (a) shows the temperature-time profile for four nodes - 3 nodes located above each defect and the 4th one on the defect-free region. Figure 3.9 (b), 3.9 (c), and 3.9 (d) show the change in the temperature with respect to frames, logarithmic scale of the cooling curve and logarithmic scale after skipping 700 frames respectively.

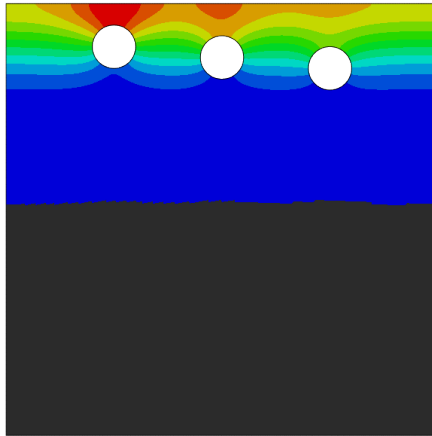


Figure 3.8: Defect located 100 μm , 150 μm , 200 μm from the top surface from left to right.

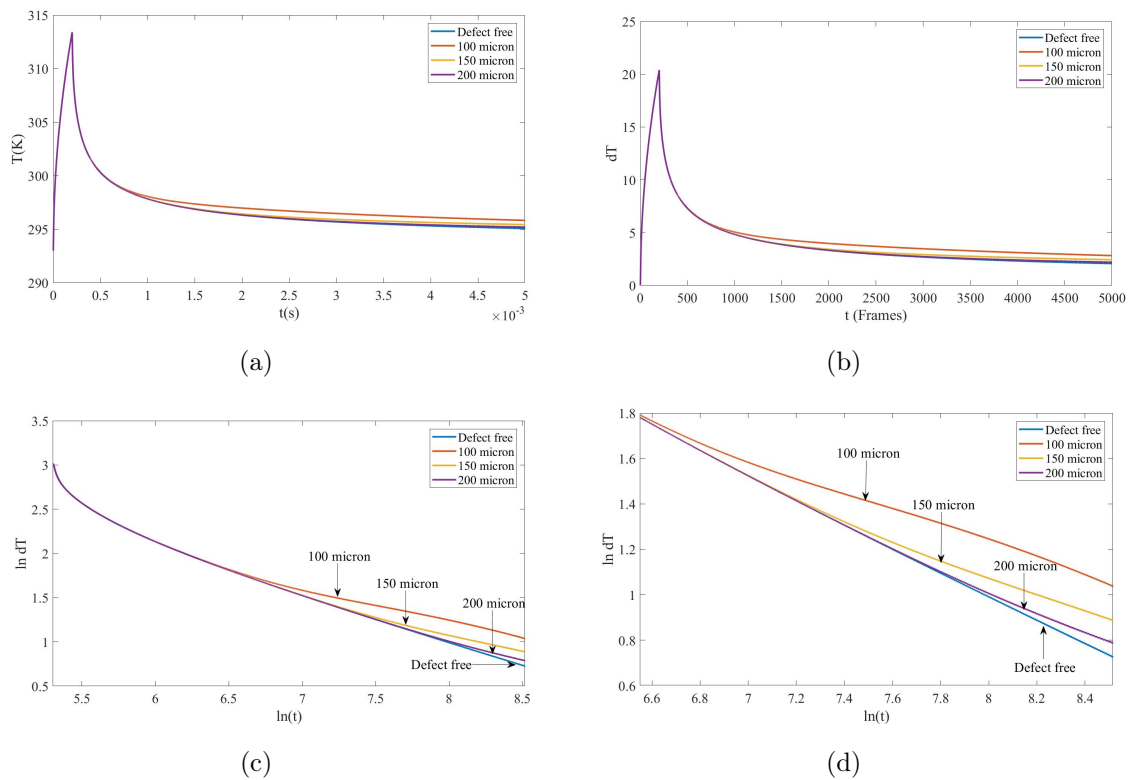


Figure 3.9: (a) Comparison of temporal variation of temperature for four nodes on the surface. (b) Plot of change in temperature w.r.t time(frames) for those same nodes. (c) Logarithmic scale. (d) Logarithmic plot after skipping post flash frames.

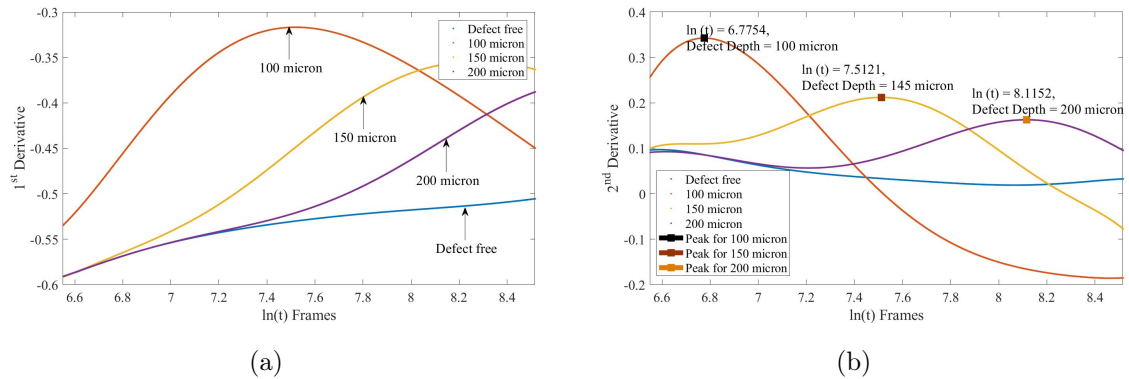


Figure 3.10: (a) 1st derivative plot of 8th order polynomial. (b) 2nd derivative plot of 8th order polynomial.

In the study depicted in Figure 3.10 (a) and 3.10 (b), the order of polynomial was kept constant for all the defects to see if it can give accurate defect location. It was observed that the curve fitting parameters used in section 3.3 failed to quantify the defects in this study. However, the 6th order polynomial was successful in predicting the defect that was at 100 μm and 200 μm from the top but it failed to give a correct estimate for the defect that was 150 μm from the top. Therefore, a higher order polynomial was chosen. The 7th order polynomial gave the same result as the 6th order polynomial. However, the 8th order polynomial gave an accurate defect location for the 100 μm , 150 μm and 200 μm as shown in figure 3.10 (b). Moreover, the second derivative peaks gave an approximate estimation of the correct depth of the defect.

These studies concluded that the TSR technique has challenges in terms of selecting the order of polynomial and the number of post-flash frames to be skipped. The results vary depending on these two factors. Also, it is only valid for the flash duration that is smaller than the diffusion time for the heat flux to reach the defect. Hence, there is a need for another technique that accounts for these factors. The coefficient maps approach takes the non-uniformity in the flash heating into consideration, and it is independent of the curve-fitting polynomials.

CHAPTER 4: COEFFICIENT MAPS

4.1 Background

The exact solution of governing a differential heat conduction equation for a semi-infinite plate with a surface heat flux of the form Dirac delta function and insulated boundary condition is given by Equation (2.5) and the log form is [7]:

$$\underbrace{\log(\Delta T)}_y = \underbrace{-0.5}_{c} \overbrace{\log(t)}^x + \underbrace{\log\left(\frac{Q}{\sqrt{e\pi}}\right)}_b \quad (4.1)$$

The surface temperature decreases as a square root of time for a defect-free artifact. The equation above can be compared with the equation of a straight line $y = cx + b$ (where c is the slope and b is the intercept) and the change in the slope from -0.5 signifies the presence of any discontinuity in the artifact. In practice, the slope is not the same as that of the theoretical value because the heat source is not of the form of a Dirac delta function, but there is a relative difference between the slope of the defect and the defect-free region on the surface. Also, this equation is valid for semi-infinite material, but since AM parts have very little thickness, the slope may differ from -0.5 .

4.1.1 Analytical solution for semi-infinite and finite width plate for square pulse-heat source

The most common heat source considered in flash heating is a pulse. In flash thermography, the flash is turned on for a few milliseconds to impart the energy sufficient enough to raise the temperature of the specimen under inspection. All the simulations done in this work are based on a square heat-pulse. Also, in an in-situ measurement, the measurement is taken after melting a few layers of the AM part, so

the approximation of semi-infinite material is not appropriate. Hence, for the purpose of modeling, the thickness of the artifact is considered as a finite thickness.

The analytical solution for a semi-infinite plate with an insulated boundary condition and heat flux of the form of a square pulse is given by

$$\Delta T_s^\infty(0, t) = \frac{2Q}{\rho e \sqrt{\pi}} \left\{ \sqrt{t} [\mathcal{H}(t) - \mathcal{H}(t - \tau)] + (\sqrt{t} - \sqrt{t - \tau}) \mathcal{H}(t - \tau) \right\} \quad (4.2)$$

where, Q is the heat energy (J/m^2), τ is the duration of the heat flux (s), and \mathcal{H} is the Heaviside function.

The analytical solution for finite width plate with an insulated boundary condition and heat flux of the form of a square pulse is given by

$$\Delta T_s^f(0, t) = \frac{Q}{\rho C_p L \tau} \left\{ t \mathcal{H}(t) - (t - \tau) \mathcal{H}(t - \tau) + \sum_{n=1}^{\infty} \frac{2}{\alpha \lambda_n^2} \left[\left(1 - e^{-\alpha \lambda_n^2 t} \right) \mathcal{H}(t) - \left(1 - e^{-\alpha \lambda_n^2 (t - \tau)} \right) \mathcal{H}(t - \tau) \right] \right\} \quad (4.3)$$

where L = thickness of the plate (m) and $\lambda_n = \frac{n\pi}{L}$.

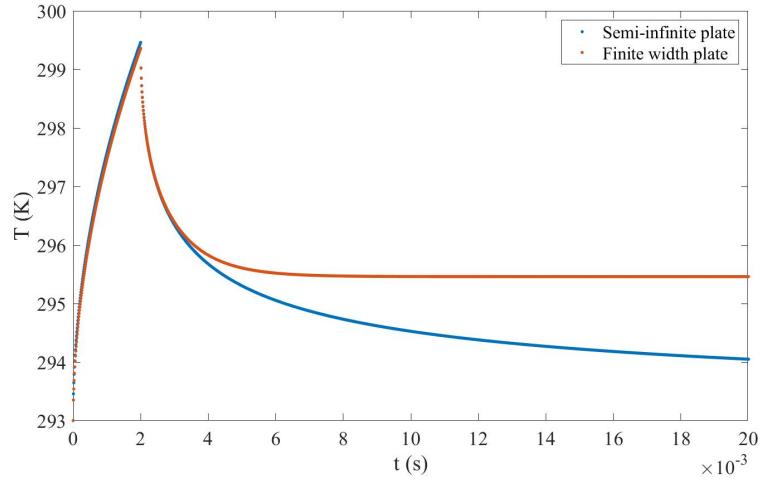


Figure 4.1: Comparison of Semi-infinite and finite plate thickness.

Figure 4.1 compares the analytical models of the semi-infinite plate and the finite plate of SS-316l of 0.2 mm thickness with a square pulse of duration 2 ms. This graph gives insight into the temperature decay on the surface for finite and semi-infinite

material. The deviation observed in the finite width curve from the semi-infinite curve is due to the heat reaching the back wall of the sample. In the case of the semi-infinite plate, the material is thick enough not to affect the back wall; hence the temperature decay continues at a higher rate. Both the curves reach back to room temperature (293 K) after some time, but the heat propagation in the finite plate takes a little longer to reach room temperature.

4.1.2 Comparison of analytical and numerical solution for finite width plate

The numerical model was validated by comparing the temperature-time profile with the analytical solution for a finite plate of SS-316l with square pulse heat flux. The numerical solution was obtained using ABAQUS Explicit. A plate with dimensions $2 \text{ mm} \times 2 \text{ mm} \times 0.2 \text{ mm}$ was given the property of SS-316l (mentioned in Table 4.2) with insulated boundary conditions and time step of $10 \text{ } \mu\text{s}$. The heat flux of magnitude 1 MW/m^2 is applied on the top surface for 2 ms.

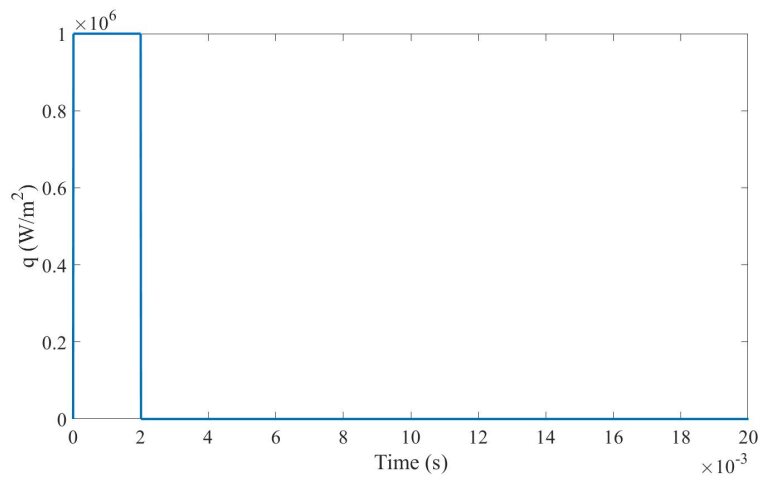


Figure 4.2: Square pulse heat flux.

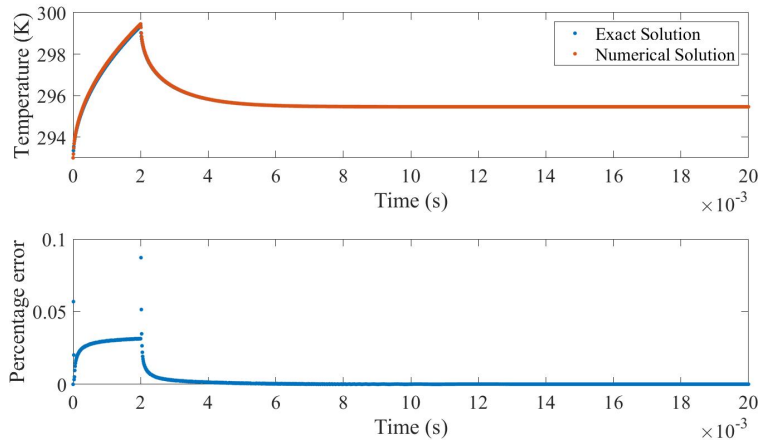


Figure 4.3: Exact and Numerical solution.

The analytical and numerical solution plots shown in figure 4.3 validates the accuracy of the numerical model. According to the percentage error plot shown along with the temperature-time profile, there is a slight difference in the numerical solution and the analytical solution when the heat flux is applied on the top surface. However, they closely agree when the heat flux is turned off, and the sample is cooling. The error is because of the mesh size and the time increment used in the numerical analysis. By decreasing the time increment and the mesh size, the percentage error can be further minimized.

4.2 Boundary Conditions

Heat transfer problems stem from three boundary conditions: insulation, convection and radiation. To closely approximate the actual flash thermography measurement, it is trivial to consider the effect of each boundary condition on the surface temperature. An FEA was carried out to compare the effect of each boundary condition on the temperature distribution for a defect-free artifact. The simple geometry shown in figure 4.4 is a typical specimen taken under consideration for this study. The surface heat flux on the top surface is of the magnitude 1 MW/m^2 for 2 ms and the sample is allowed to cool down for the next 18 ms.

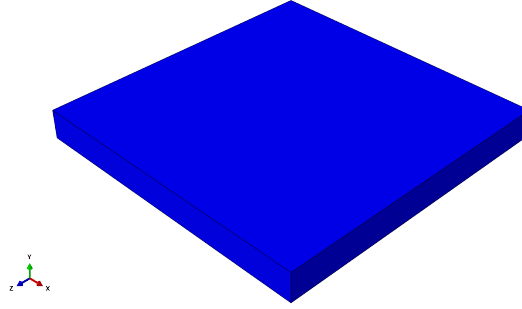


Figure 4.4: FEA model for defect free sample.

Table 4.1: General boundary condition equation for 1D heat conduction problem

Boundary Condition	Equation
Insulated	$-k \frac{\partial T}{\partial t} \Big _{x=0} = 0$
Convection	$-k \frac{\partial T}{\partial t} \Big _{x=0} = h[T_{\infty} - T(0, t)]$
Radiation	$-k \frac{\partial T}{\partial t} \Big _{x=0} = \sigma \epsilon [(T(0, t) - T_{abs})^4 - (T_{\infty} - T_{abs})^4]$

For this study, the individual effect of boundary conditions is studied. Firstly, the insulated boundary condition is simulated considering no heat flux is leaving through the boundaries. For convection, the bottom surface is considered insulated, while the top and lateral surfaces are given a convective heat transfer coefficient of $h = 100 \text{ W/m}^2$ and a surrounding temperature of $T_{\infty} = 293 \text{ K}$. Lastly, for the radiation boundary condition, the top surface is given emissivity of $\epsilon = 0.45$ [23] and the Stefan-Boltzmann constant ($\sigma = 5.67 \times 10^{-8} \text{ W/m}^2\text{K}^4$). The lateral surfaces are also given a convective boundary condition.

Figure 4.5 shows the results of the simulation for all three cases. The temperature-time profile for a node centrally located on the surface is shown in the figure below. There is hardly any variation in the temperature distribution for all three cases. A zoomed-in graph within the main plot shows that because of the heat loss due to convective and radiation boundary conditions, the maximum temperature for an insulated boundary condition is slightly higher than the other two cases.

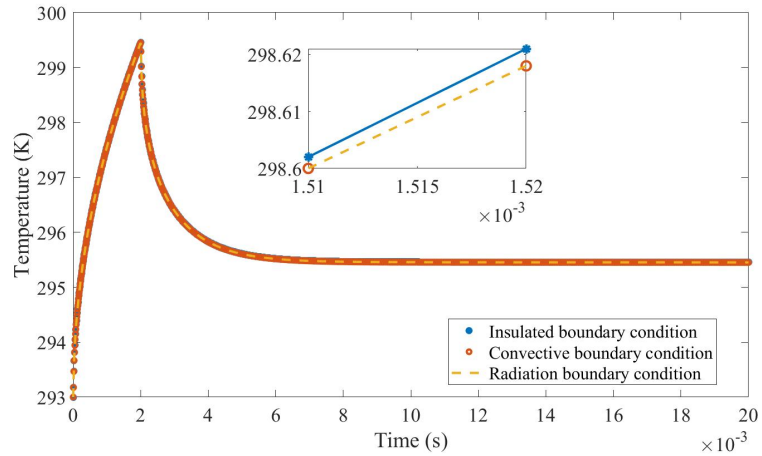


Figure 4.5: Effect of boundary condition on temperature distribution.

4.3 Introduction Of Defect

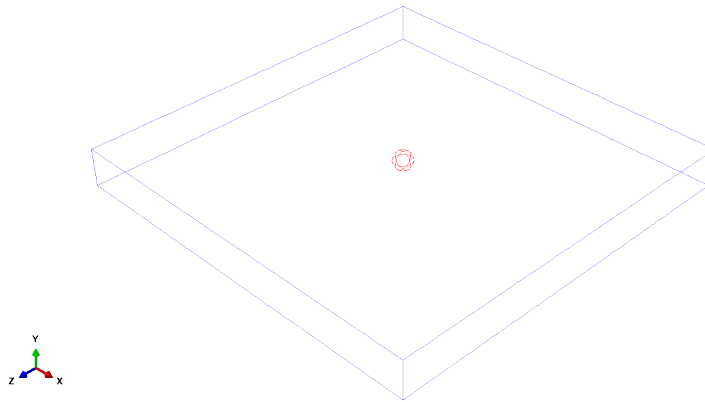


Figure 4.6: Air inclusion in the SS-316l block.

A finite element model is developed in ABAQUS with a single defect, centrally located. The depth of the defect is changed, and the effect is observed on the c -map and b -map. A spherical defect with a diameter of $100 \mu\text{m}$ is placed in the SS-316l block. The defect is considered as an air inclusion with the following properties:

Table 4.2: Thermal Properties of Air [1]

Thermal conductivity (χ) (W/mK)	Density (ρ)(kg/m ³)	Specific Heat Capacity (C_p) (J/kg K)
0.026	1.177	1005

The red section in figure 4.6 represents a defect, i.e., air bubble located centrally in the 2 mm \times 2 mm \times 0.2 mm block of SS-316l. The heat flux of magnitude 0.1 MW/m² is applied on the top surface for 2 ms and the simulation runs for 20 ms. The defect is located 10 μ m from the top surface. The heat diffusion simulates a 1D heat diffusion model until the heat reaches the defect. The heat transfer rate is affected, and a hot-spot appears on the top surface which signifies the presence of some discontinuity in the block. The region away from the defect will have a 1D heat diffusion because the defect does not affect temperature distribution after a certain distance.

The temporal variation of the temperature for all the nodes on the top surface is recorded and exported to Matlab for post-processing. The data from first 2 ms is neglected since the heat flux is still on and only the cooling curves are observed to recreate the surface. A logarithm of the change in temperature is calculated and plotted against the logarithm of frame numbers for all the nodes. Then a linear portion of the log scale is curve fitted with a polynomial of the form $f(x) = cx + b$ (c is the slope or c -map and b is the intercept or b -map). These coefficients are obtained for all the nodes, and a surface is passed through them using `griddata`. If discoloration is observed in the center, it signifies the presence of a defect.

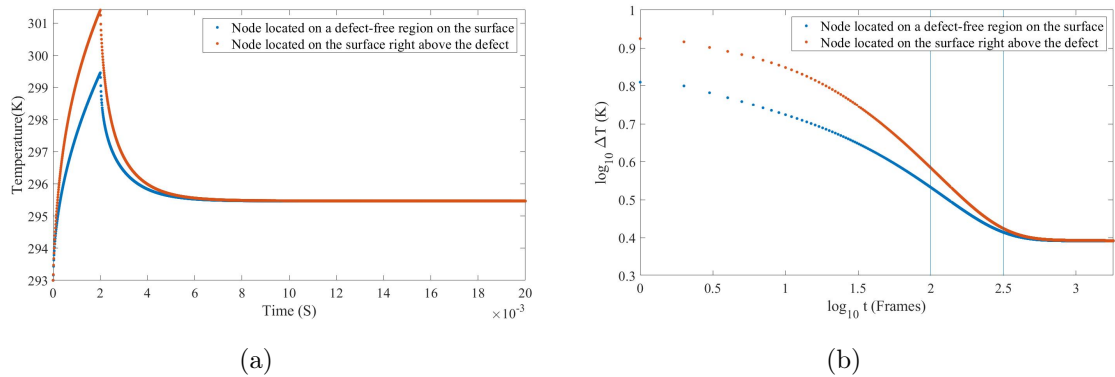


Figure 4.7: (a) Temporal variation of temperature for two nodes. (b) Logarithmic scale of change in temperature w.r.t frames.

Figure 4.7(a) shows the plot of temperature vs. time profile for two nodes located on the top surface. The temperature of the node closer to the defect is higher compared to the node far away from the defect because of the heat accumulation over the defect. The logarithmic scale, shown in figure 4.7 (b) scales the temperature data and amplifies the signal. The non-linearity observed in the beginning is because of the sudden temperature drop occurring due to shut down of the heat source. Since a first-order polynomial is used for approximating the data in the logarithmic scale, a linear region is identified in the log-log plot for curve fitting. The approach is to avoid the non-linearity in the beginning because that gives a sparse approximation of the data. The two vertical lines in the logarithmic scale show the linear region of the curves. Curve fitting the linear region gives two coefficients c and b for all the nodes on the top surface.

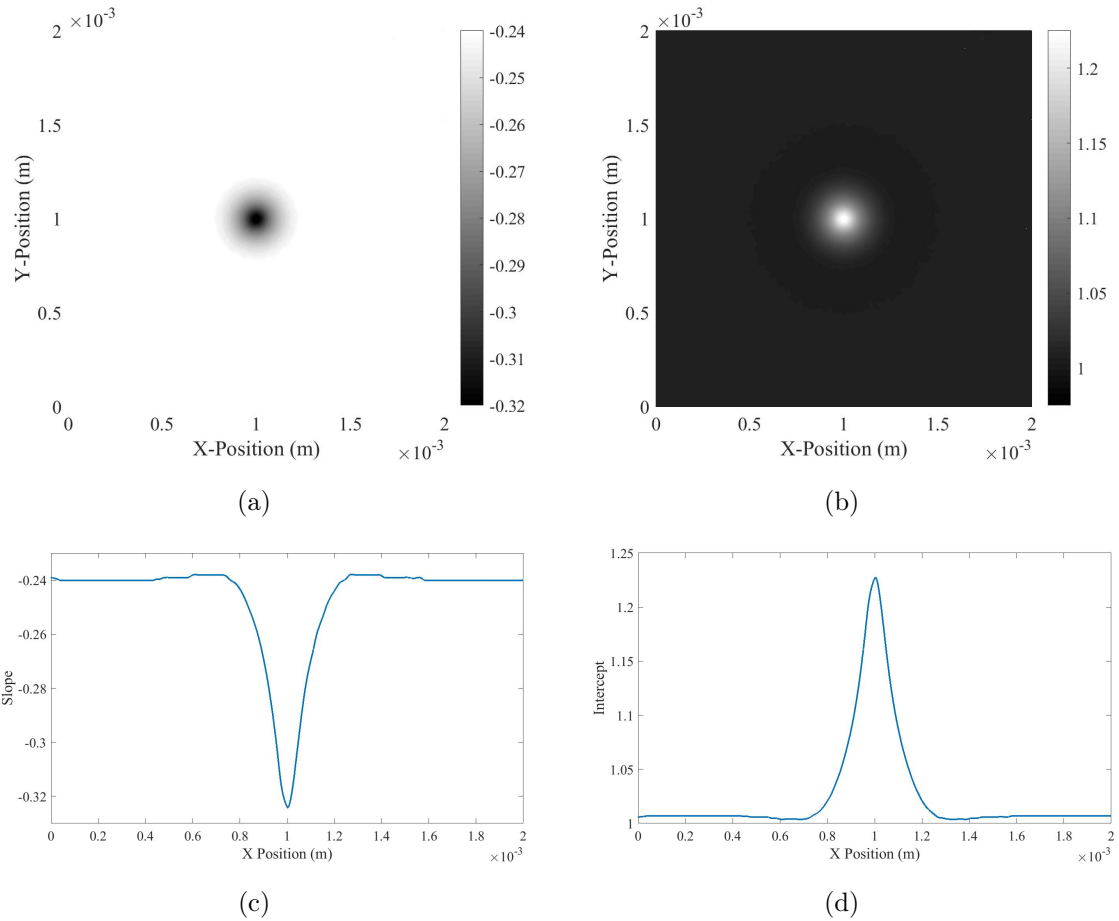


Figure 4.8: (a) *c*-map (b) *b*-map. (c) Plot of slope vs x-position. (d) Plot of intercept vs x-position.

The slope and intercept calculated for each node are plotted against their respective node location to generate the surface map. A surface fit through those data gives a *c*-map and a *b*-map as shown in figure 4.8(a) and figure 4.8(b). The contrast in the *c*-map and *b*-map is an indication of a sub-surface defect. Figure 4.8(c) and figure 4.8(d) are the magnitude of slope and intercept along the center line. A deviation in the magnitude of slope and intercept is observed in the center because of the air inclusion. The magnitude of the slope is the same everywhere but the center which signifies the presence of any discontinuity in the material.

4.4 Defect At Varying Depth

The depth of the defect is changed in the above model to study the changes in the temperature-time profile, log-log plot, c -map and b -map. Here four cases are considered. In the first case the defect is placed at $10\ \mu\text{m}$ deep from the top surface, for second, third and fourth cases, the defect is placed at $25\ \mu\text{m}$, $50\ \mu\text{m}$ and $100\ \mu\text{m}$ respectively from the top surface. The heat conduction process is affected by changing the depth of the defect. For the near surface defect, the diffusion time is shorter than the defect far from the top surface. Due to shorter diffusion time, the relative temperature rise for a near surface defect is significantly higher than the defect far from the surface.

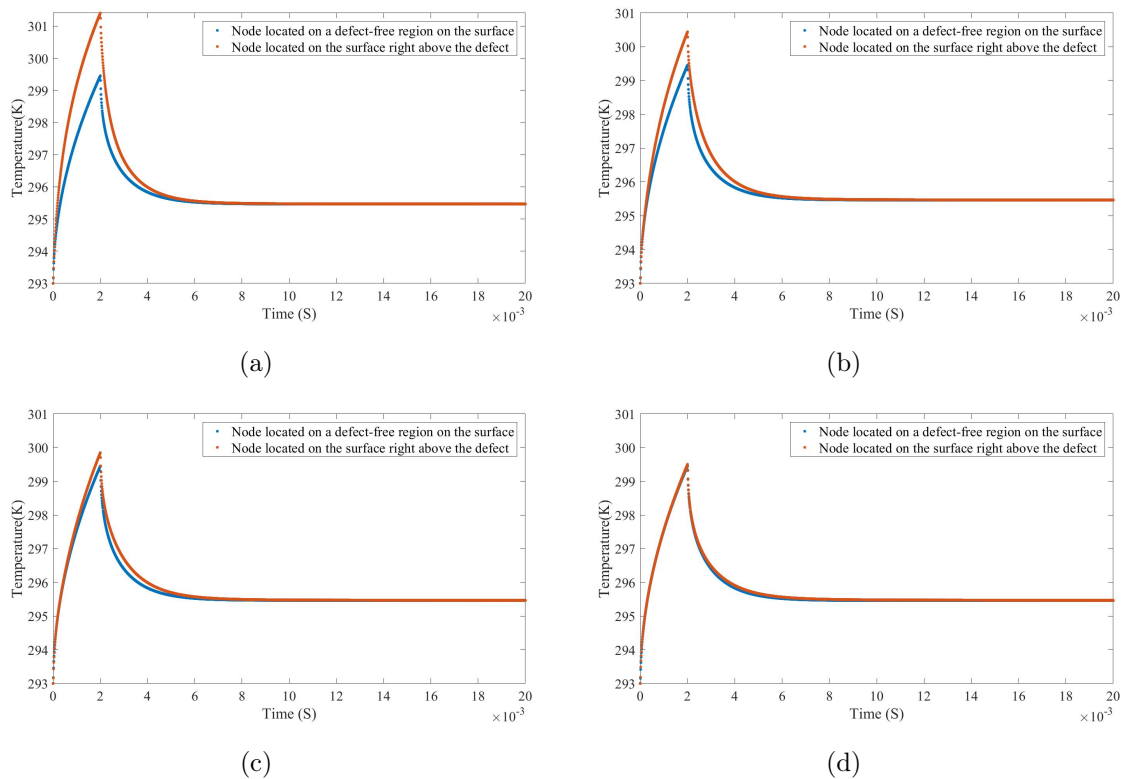


Figure 4.9: Temporal variation of temperature for a defect located at (a) $10\ \mu\text{m}$ deep. (b) $25\ \mu\text{m}$ deep. (c) $50\ \mu\text{m}$ deep. (d) $100\ \mu\text{m}$ deep.

It is evident from the temperature-time profile shown in figure 4.9 that the peak temperature for the node over the defect differs for all four cases. The temperature-

time profile of the defect-free node is the same for all the four cases because it is unaffected by the presence of the defect. There is a simple 1D heat diffusion for these nodes. Changing the depth of the defect, from 10 microns to 100 microns, the thermogram moves towards a 1D heat diffusion model. This is because the heat energy reaches the bottom surface and redistributes itself for the given thickness of the block. Also, the air inclusion at a depth of 100-microns is touching the bottom surface; hence that is too far from the top surface making it challenging to capture the defect in the thermograms. The logarithmic scale shown in figure 4.10 signifies the presence of the defect by scaling the data. The strongest signal is observed for the 10-micron defect. The logarithm of the defect node is easily distinguishable from the defect-free node. This difference keeps on decreasing as the defect moves far from the surface.

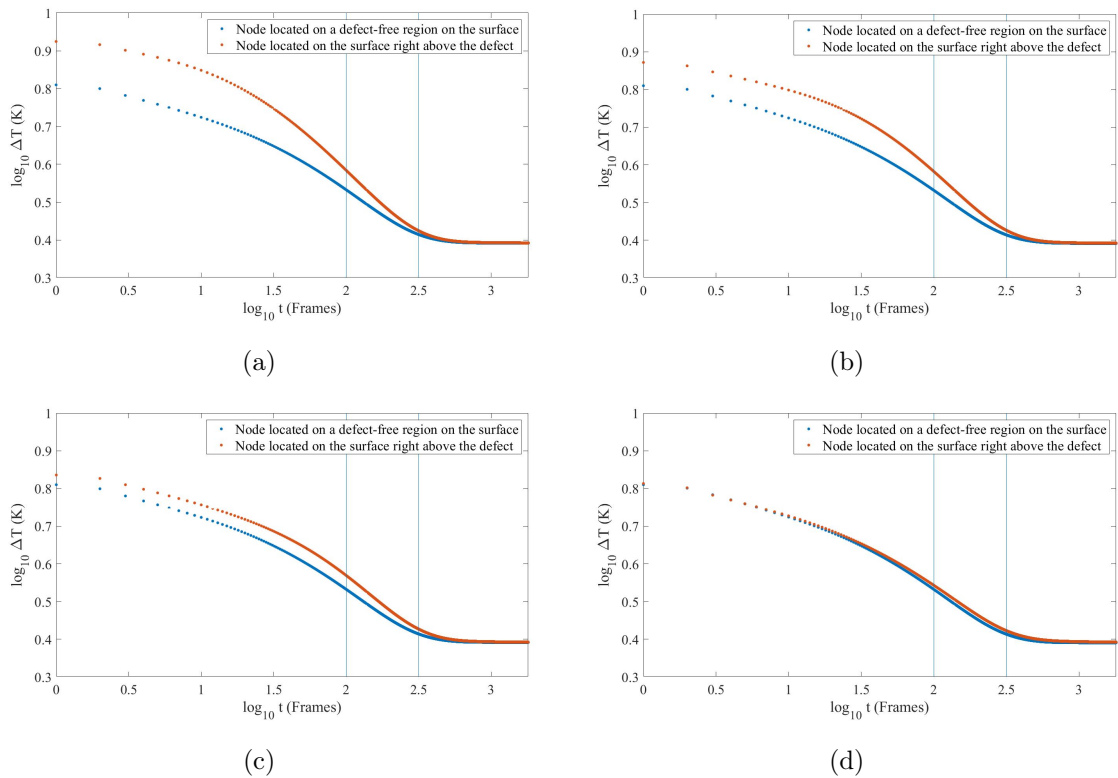


Figure 4.10: Logarithmic scale of temperature profile for a defect located at (a) 10 μm deep. (b) 25 μm deep. (c) 50 μm deep. (d) 100 μm deep.

Figure 4.11 and 4.12 shows the defect maps for each case with their respective magnitudes along the side. Here the color bar is kept constant for all the cases to show the effect of the defect being faded away with the increase in depth. It is not standard practice, but it is done for comparison. The cooling rate of the non-defect node is higher than the defect node because of the absence of any obstruction in heat conduction. Thus, the magnitude of the slope for the defect-free node is higher than the defect node. Figure 4.11 (b) shows the magnitude of slope vs. x-position in which the magnitude of the slope decreases in the center because of the presence of the defect. As the defect moves away from the surface, the difference in the logarithmic scale starts to decrease. Hence, in the figure 4.11 (h), the magnitude of the slope for the defect-free region and defective region is almost the same. The same trend is observed in the b-maps in figure 4.12 just the magnitude is different, and the y-intercept is positive because the temperature is decreasing.

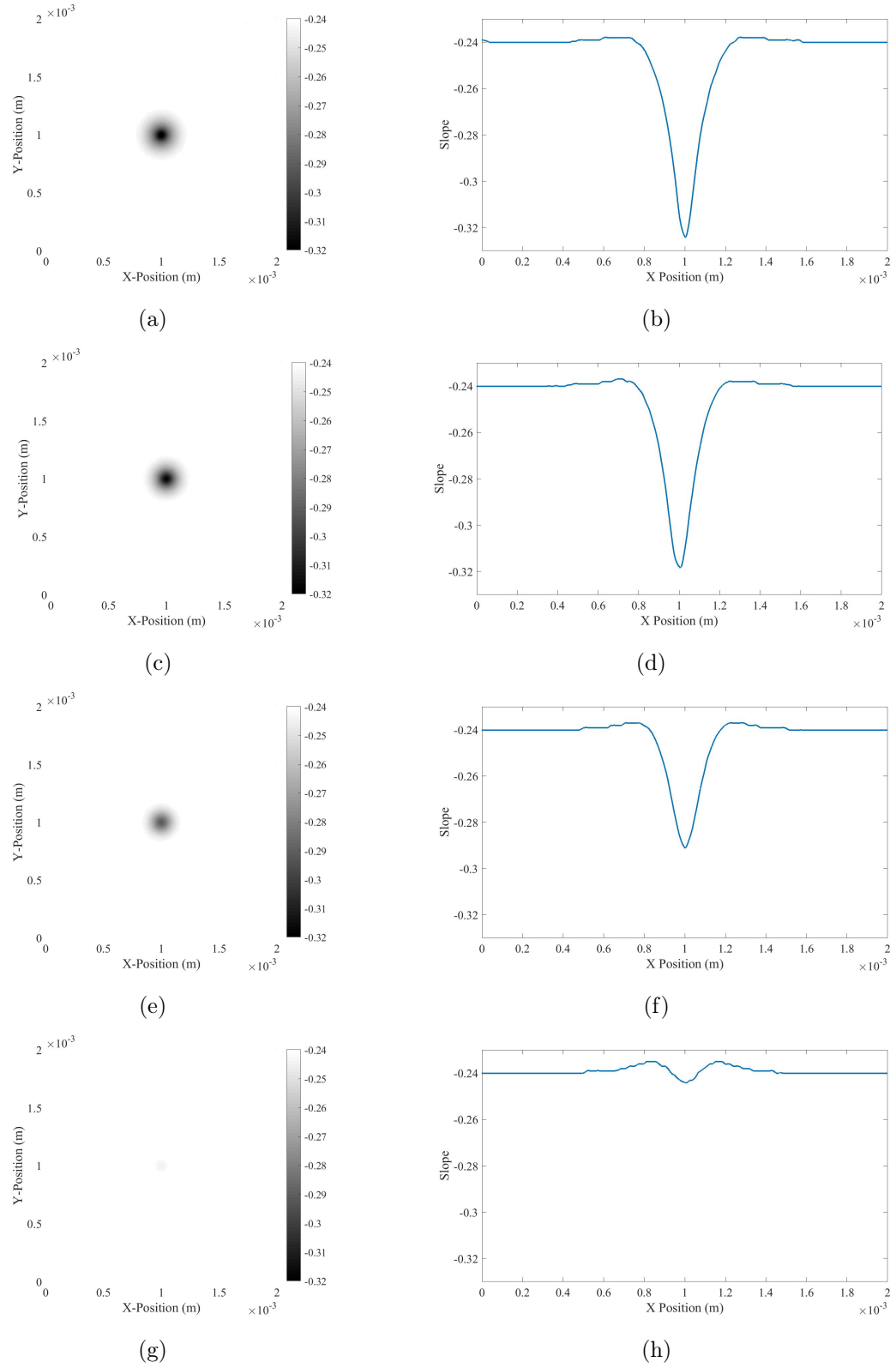


Figure 4.11: *c*-maps and magnitude of slope w.r.t position for a defect located at (a), (b) 10 μm deep. (c), (d) 25 μm deep. (e), (f) 50 μm deep. (g), (h) 100 μm deep.

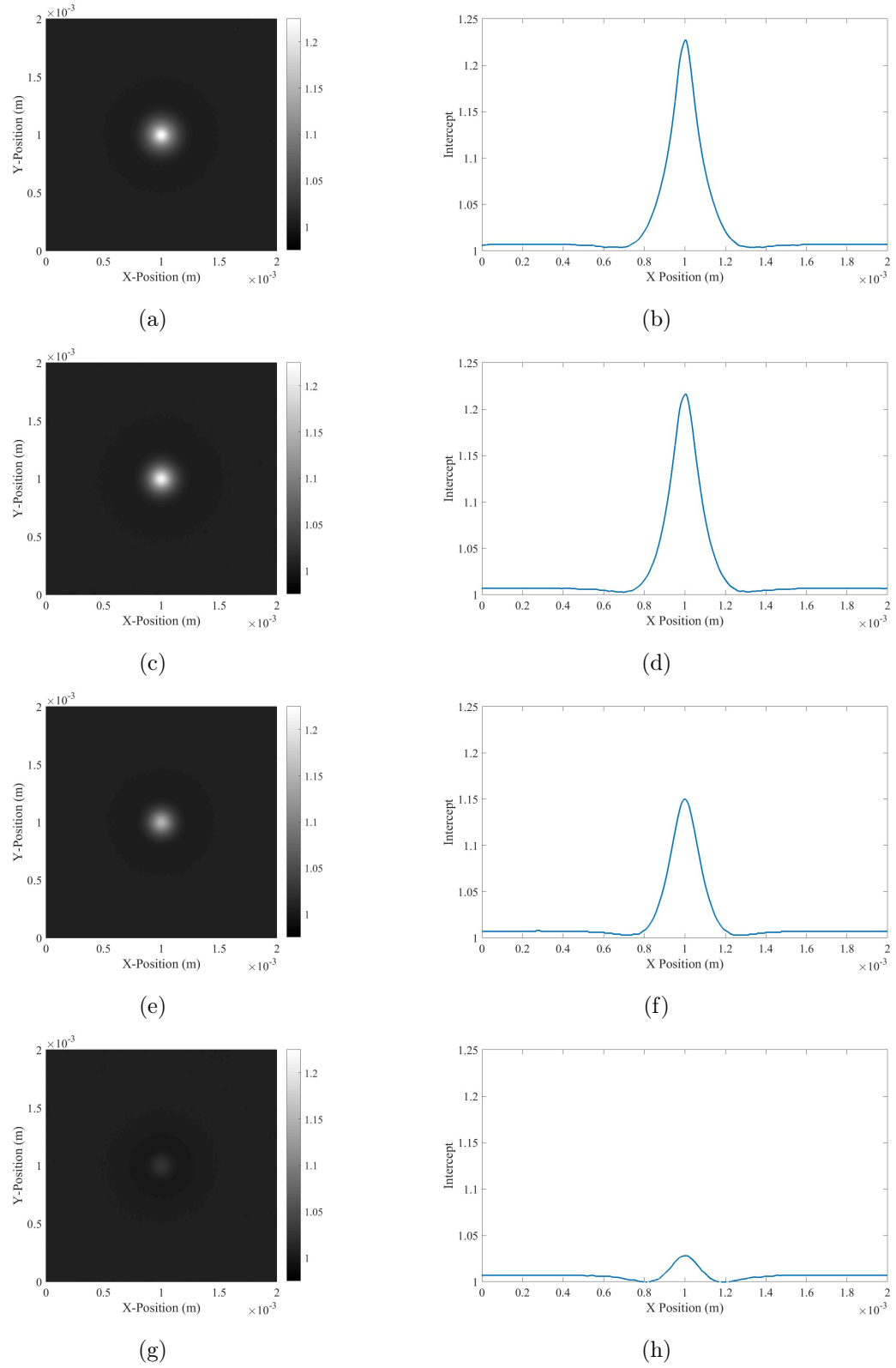


Figure 4.12: b -maps and magnitude of intercept w.r.t position for a defect located at (a), (b) 10 μm deep. (c), (d) 25 μm deep. (e), (f) 50 μm deep. (g), (h) 100 μm deep.

4.5 Multiple Defects In A Row

Modeling one defect gave insight on the principal of heat conduction in FT. However, when there is more than one defect, the heat diffusion through the bulk will change in the vicinity of the defects. Factors such as defect location and distance between two defects influence the temperature distribution over the top surface. In this section, three different models are studied to illustrate the heat diffusion process when there are two defects beside each other, multiple defects in a row at a different distance and multiple defects in a row equidistant from each other.

4.5.1 Modeling of two inline defects

A new model has been developed with two defects of spherical shape with $\varphi 100\ \mu\text{m}$. As shown in figure 4.13, both defects are placed next to each other to study their effect on heat conduction, specifically the effect of convection. The dimensions of the block are the same as those mentioned in the above section. Keeping the rest of the modeling parameters same as used in the previous sections, the simulation was run for 20 ms with an addition of radiation on the top surface and convection on the lateral surfaces.

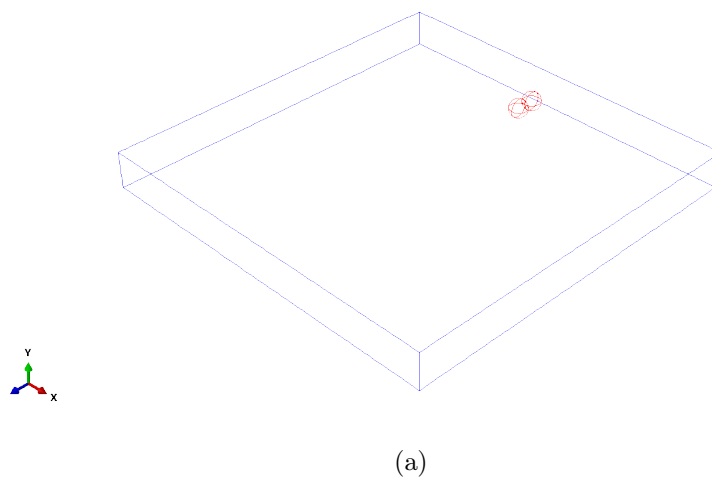


Figure 4.13: Schematics of two defects placed together at $50\ \mu\text{m}$ beneath the top surface in SS-316l block.

A larger surface area will have a different temperature gradient because of the presence of two defects having low thermal conductivity compared to the parent material. Having both defects, side by side, makes the heat diffusion process much slower thereby reducing the cooling rate of the nodes above the defect. In case of a single spherical defect, there was one circular hot spot over the defect, but with two inline defects, the hot spots will overlap resembling an ellipse on the surface.

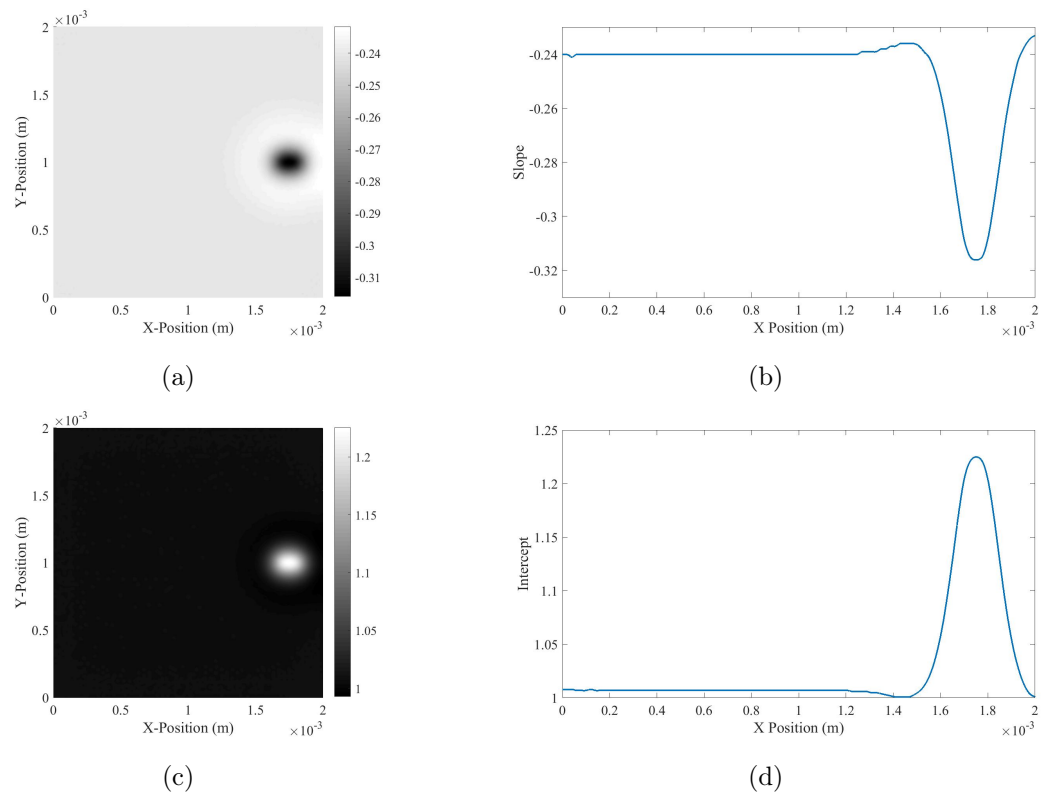


Figure 4.14: (a) *c*-map for two inline defects. (b) Magnitude of slope w.r.t. x-position. (c) *b*-map for two inline defects. (d) Magnitude of intercept w.r.t x-position

Figure 4.14 shows the *c*-map and *b*-map with their magnitudes on the right. The magnitude of the slope and the intercept is much lower than the case with a single defect. The halo observed around the hot spot is due to the heat dispersion around the defect. It is difficult to characterize the defect based on the elliptical hot spot because it can be argued that there is one non-spherical defect large enough to make the elliptical hot spot. To assert the presence of two defects, we need two distinct

signals or two hot spots to confirm the presence of two defects. This ambiguity can be avoided when the defects are separated by a significant distance.

4.5.2 Media with multiple defects at varying distance

Multiple defects of the same size ($\phi 100 \mu\text{m}$), each located 10 microns from the top surface are shown in figure 4.15 (a). The cross-sectional view shown in figure 4.15 (b) display the distance between each defects. Each air inclusions are separated by an incremental distance of 100 microns from right to left. The boundary conditions, the initial condition and the surface heat flux used in the models above is kept the same for this model.

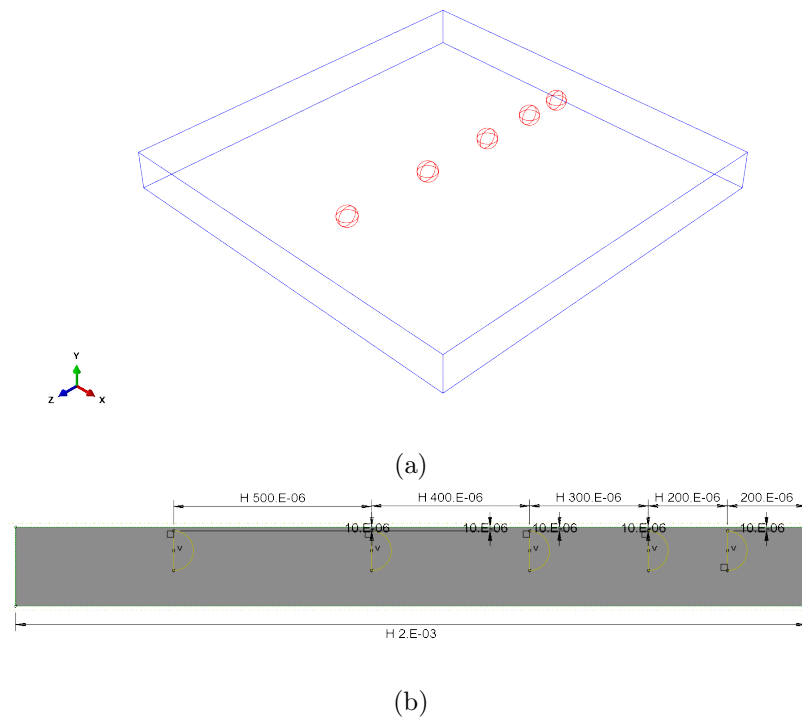


Figure 4.15: (a) Schematics of multiple defects placed together at $10 \mu\text{m}$ beneath the top surface. (b) Sectional view.

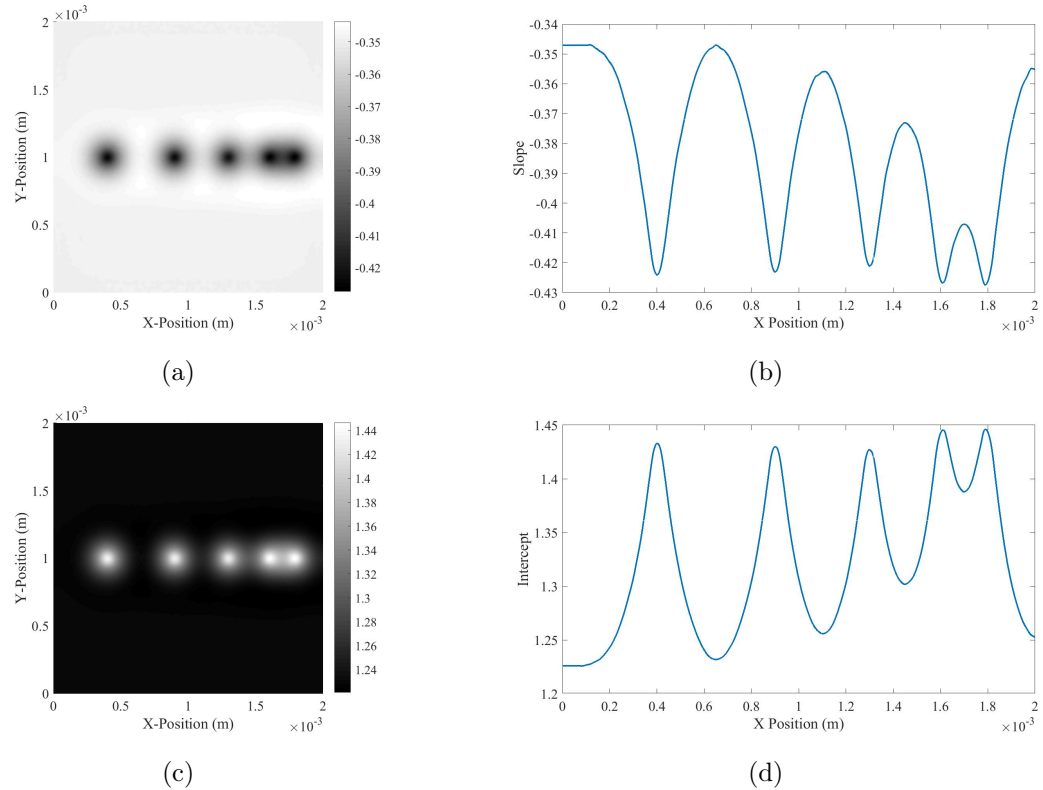


Figure 4.16: (a) *c*-map for multiple defects. (b) Magnitude of slope w.r.t. x-position. (c) *b*-map for multiple defects. (d) Magnitude of intercept w.r.t x-position.

On analyzing the *c*-map and *b*-map for multiple inline defects as shown in figure 4.17, it is clear that when two defects are too close to each other, it is difficult to differentiate them as two individual defects. However, looking at the third and fourth defect from the right, it appears that when the distance of the separation is at least $300 \mu\text{m}$, the *b* and *c* maps produce two distinct signatures for each defect. At a distance of $300 \mu\text{m}$, the effect of heat dispersion is not observed which makes it easy to differentiate individual defects from each other.

4.5.3 Media with multiple defects at equidistance from each other

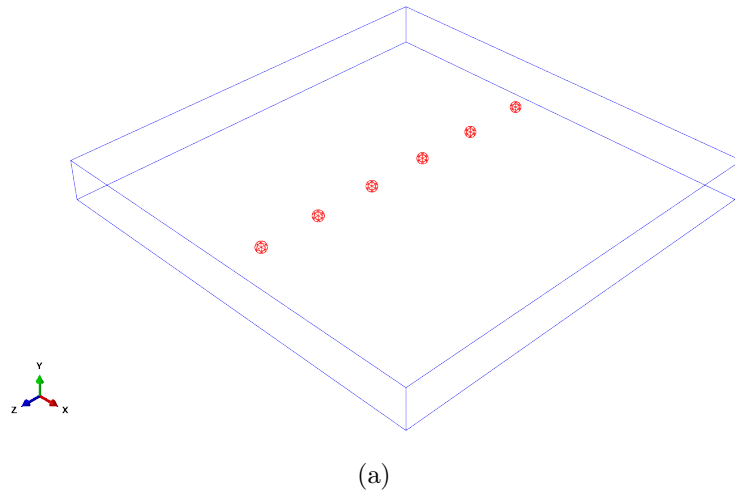


Figure 4.17: Schematics of multiple defects placed equidistant from each other, at $10\ \mu\text{m}$ beneath the top surface.

For this simulation, all the defects are modeled equidistant from each other to certify that $300\ \mu\text{m}$ should be the ideal separation gap between two defects to have a non-overlapping contrast in the c and b maps. All the defects are $10\ \mu\text{m}$ from the surface. The configuration is shown in figure 4.17. The defect maps shown in the figure 4.18 below confirms that when the defects are separated by a distance equivalent to 3 times that of the diameter of the defect, the defect maps will have a distinct signal for each discontinuity present in the artifact. This study is only limited to spherical defects. For other types of defects, the result may vary.

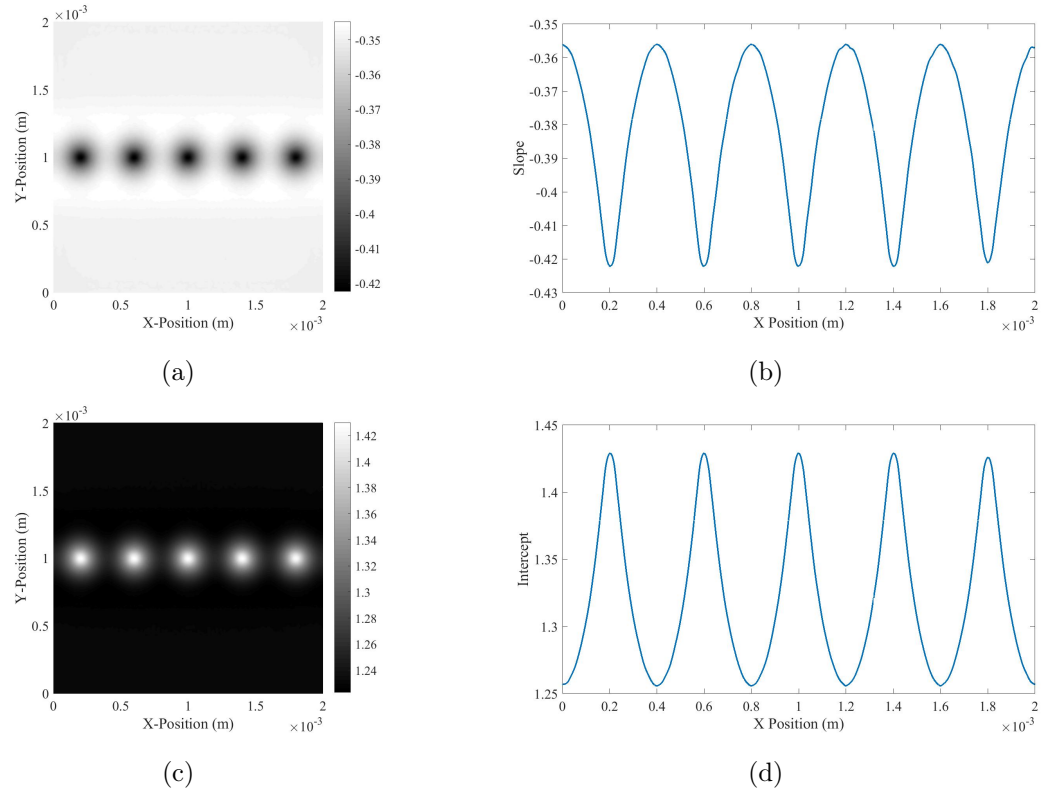


Figure 4.18: (a) c -map for multiple defects equidistant from each other. (b) Magnitude of slope w.r.t. x -position. (c) b -map for multiple defects equidistant from each other. (d) Magnitude of intercept w.r.t x -position.

4.6 Detecting Defects In Different Materials

The heat conduction process is driven by the material's thermal properties namely thermal conductivity, density, and specific heat. The rate of heat transfer depends on the thermal conductivity of the material. Materials like aluminum and copper have a high rate of heat transfer because of high thermal conductivity whereas plastics and wood have a lower rate of heat transfer because of low thermal conductivity. Thus, it is crucial to understand the response of different materials when subjected to flash heating. For this study, Ti64, Inconel and copper are analyzed to interpret their defect maps in the presence of air inclusion. Their material properties are mentioned in the table below:

Table 4.3: Material Properties of Ti64, Inconel and Copper [1]

Material Properties	Thermal Conductivity κ (W/mK)	Density ρ (kg/m ³)	Specific Heat Capacity C_p (J/kgK)	Diffusivity $\alpha = \frac{\kappa}{\rho C_p}$ (m ² /s)
Ti64	7.2	4470	560	2.88e-6
Inconel	9.8	8400	433	2.69e-6
Copper	398	8930	385	1.6e-4

4.6.1 Defect detection in Ti64, Inconel and Copper

Ti64 and Inconel are two well-known alloys in the aerospace industry where thermography is used for NDT. Their thermal conductivity is lower than SS-316l, hence with the same input of energy, Ti64 and Inconel will conduct heat at a slower rate which will result in higher peak temperatures. A comparison of FT on Inconel and Ti64 using FEA for varying defect depths is presented below. In figure 4.19 (a), the temperature vs. time profiles of defect-free nodes of both alloys for all three cases, 10 microns, 50 microns, and 100 microns is presented. The peak temperature of Ti64 is slightly higher than Inconel because of lower thermal conductivity of Ti64. The thermograms of nodes which are over the defect are shown in figure 4.19 (b) which follows the same pattern. Additionally, surface nodes that are adjacent to the defect have higher peak temperatures than the surface nodes far from the defect.

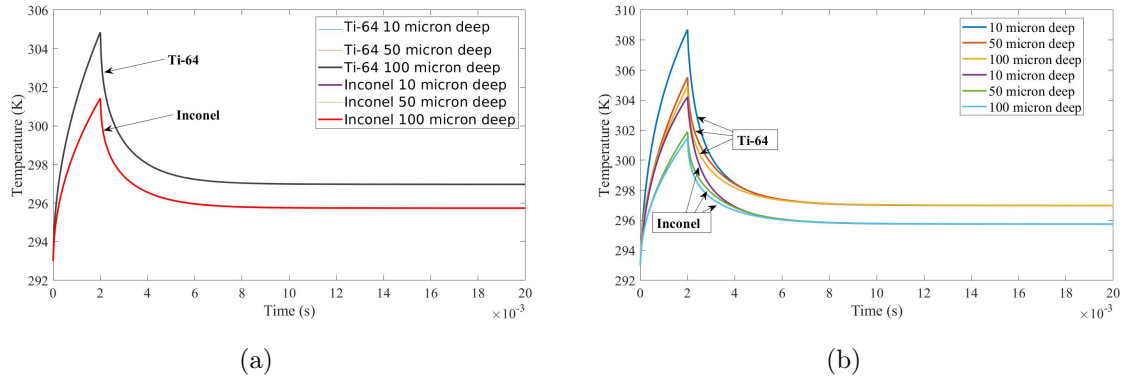


Figure 4.19: Comparison of thermograms of Ti-64 and Inconel (a) Defect-free node. (b) Node over the defect.

For both materials, the magnitudes of slopes and intercepts for all the cases are presented in figure 4.20 (a) and (b). Based on the results, it can be concluded that air inclusion at 10 μm and 50 μm from the top surface is detectable for both the materials. It is difficult to capture the 100 μm defect depth due to lower thermal conductivity reducing the heat transfer rate.

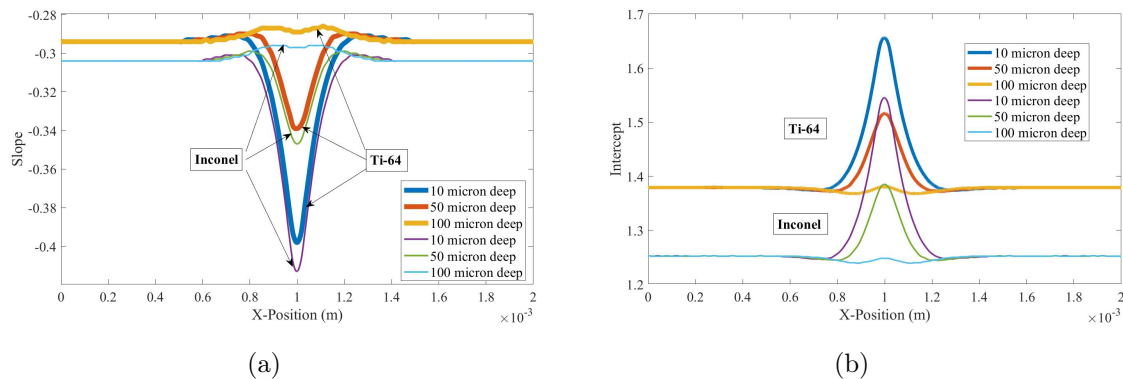


Figure 4.20: Comparison of thermograms of Ti-64 and Inconel (a) Defect-free node. (b) Node over the defect.

4.6.2 Defect detection in Copper

Copper is one of the metals with extremely high thermal conductivity and low specific heat capacity making it conduct heat at an exceptionally higher rate. This makes it challenging to capture the near-surface defects in copper because the heat

diffusion time is small. An FEA study was conducted using the material properties of copper mentioned in table 4.3. The step time for this simulation is $0.1 \mu\text{s}$.

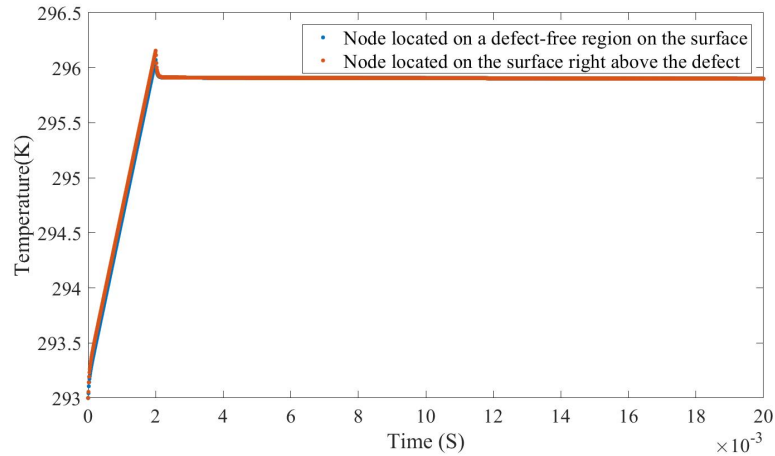


Figure 4.21: Temperature distribution of defect and defect-free node for copper.

The temperature-time profile extracted from this simulation for the defect and the defect-free node is shown in figure 4.21, which clearly shows that the cooling curves of both nodes are quite similar and have a near to zero temperature gradient. The artifact reaches the equilibrium temperature at 2.05 ms. Since there is no gradient in the cooling curve; the logarithmic scales are straight lines with a slope of 0. The defect maps fails to show any traces of air inclusion.

4.7 Comparison Based On The Depth Of The Material

A critical comparison of the magnitude of slopes and intercepts of all four materials discussed in this work is shown in figure 4.22. Vital information regarding the material properties affecting the defect maps is obtained by observing the trends in the following plots. It appears that the thermal diffusivity of the material is governing the magnitude of slopes. Inconel having the lowest diffusivity among all other materials has the smallest magnitude of slope. Increasing diffusivity starts shifting the magnitude of the slope upwards. On the other hand, the intercept is more likely affected by thermal conductivity. Ti64 has the lowest thermal conductivity, but the

magnitude of intercept is the highest. Increasing thermal conductivity decreases the magnitude of intercept. This trend is observed for spherical air defects located at a $10\ \mu\text{m}$, $50\ \mu\text{m}$ (figure 4.23) and $100\ \mu\text{m}$ (figure 4.24) depths in all four materials.

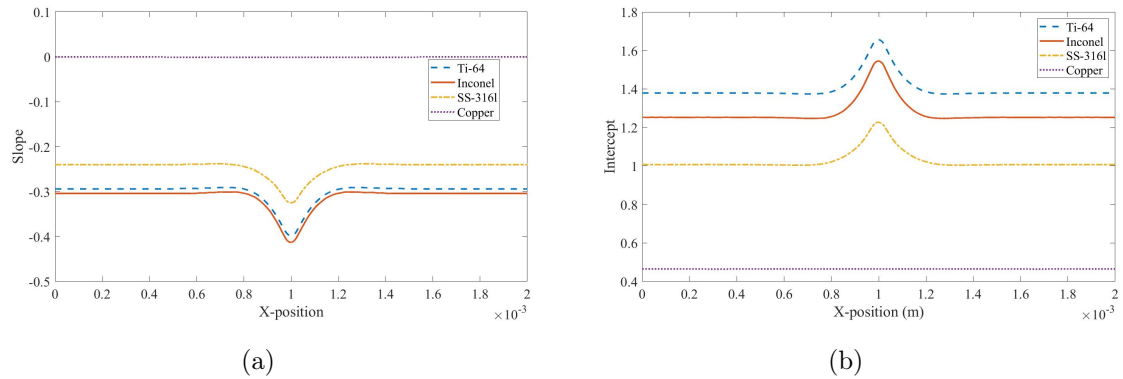


Figure 4.22: (a) Spatial variation of slope for $10\ \mu\text{m}$ deep defect. (b) Spatial variation of intercept for $10\ \mu\text{m}$ deep defect.

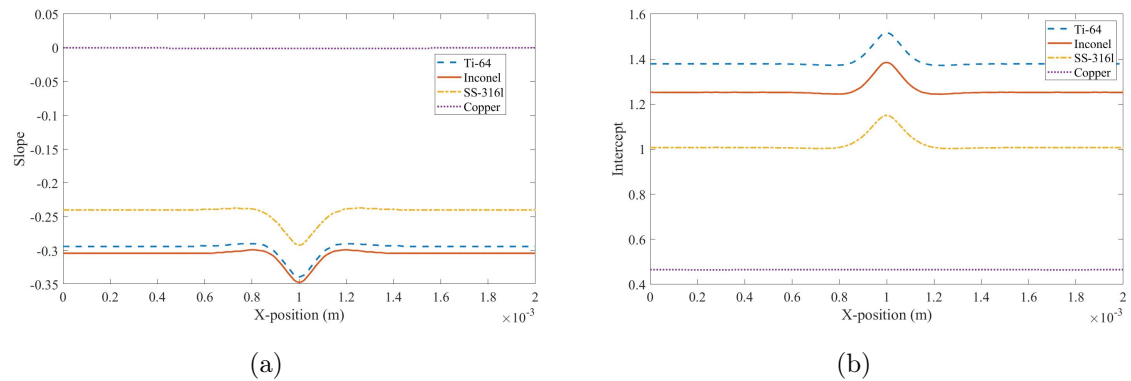


Figure 4.23: (a) Spatial variation of slope for $50\ \mu\text{m}$ deep defect. (b) Spatial variation of intercept for $50\ \mu\text{m}$ deep defect.

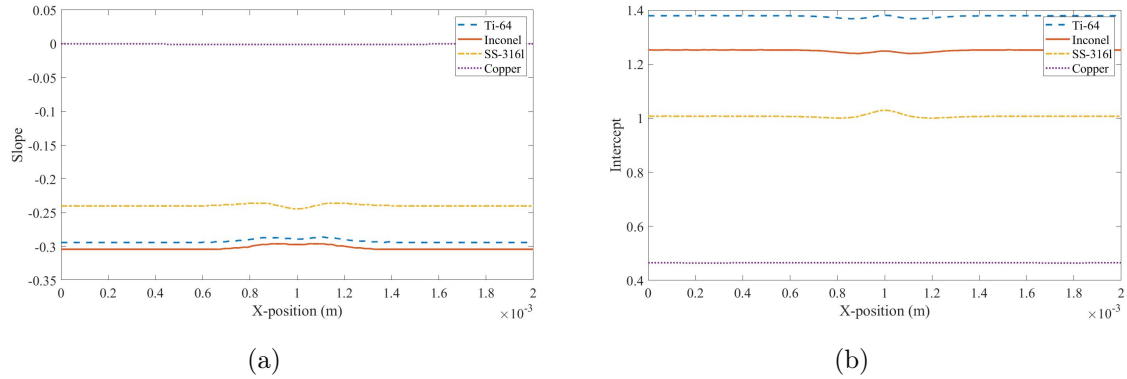


Figure 4.24: (a) Spatial variation of slope for 100 μm deep defect. (b) Spatial variation of intercept for 100 μm deep defect.

4.8 Processing The Heating Curves For Copper

The thermal decay curves of copper did not give any information about the presence of the subsurface defect because the diffusion time is short and it has a larger time-step. We decided to process the heating curves to extract the information about the presence of a discontinuity in bulk. The log scales of the temperature profile show that there is a signal or differences in the temperature gradients of the defect and defect-free node. These motivated us in analyzing the heating curves for copper. Figure 4.25 shows the simulation results for the copper block having a defect at 10 μm from the surface and is subjected to a surface heat flux of 10 MW/m^2 for 2 ms. Data is collected every 0.1 ms. The heating curve is processed using CM algorithm. There are a total of 200 data points in the heating section. A linear polynomial is fitted over 181 data points, skipping the first 19 data points because of slight non-linearity in the initial time-steps. The defect maps are shown in figure 4.25 (c) and (d) implying the presence of the defect in the center. Here, the magnitudes of the slope (figure 4.25 (e)) and intercept (figure 4.25 (f)) are opposite to that obtained from processing the cooling curve because the temperature is increasing with time.

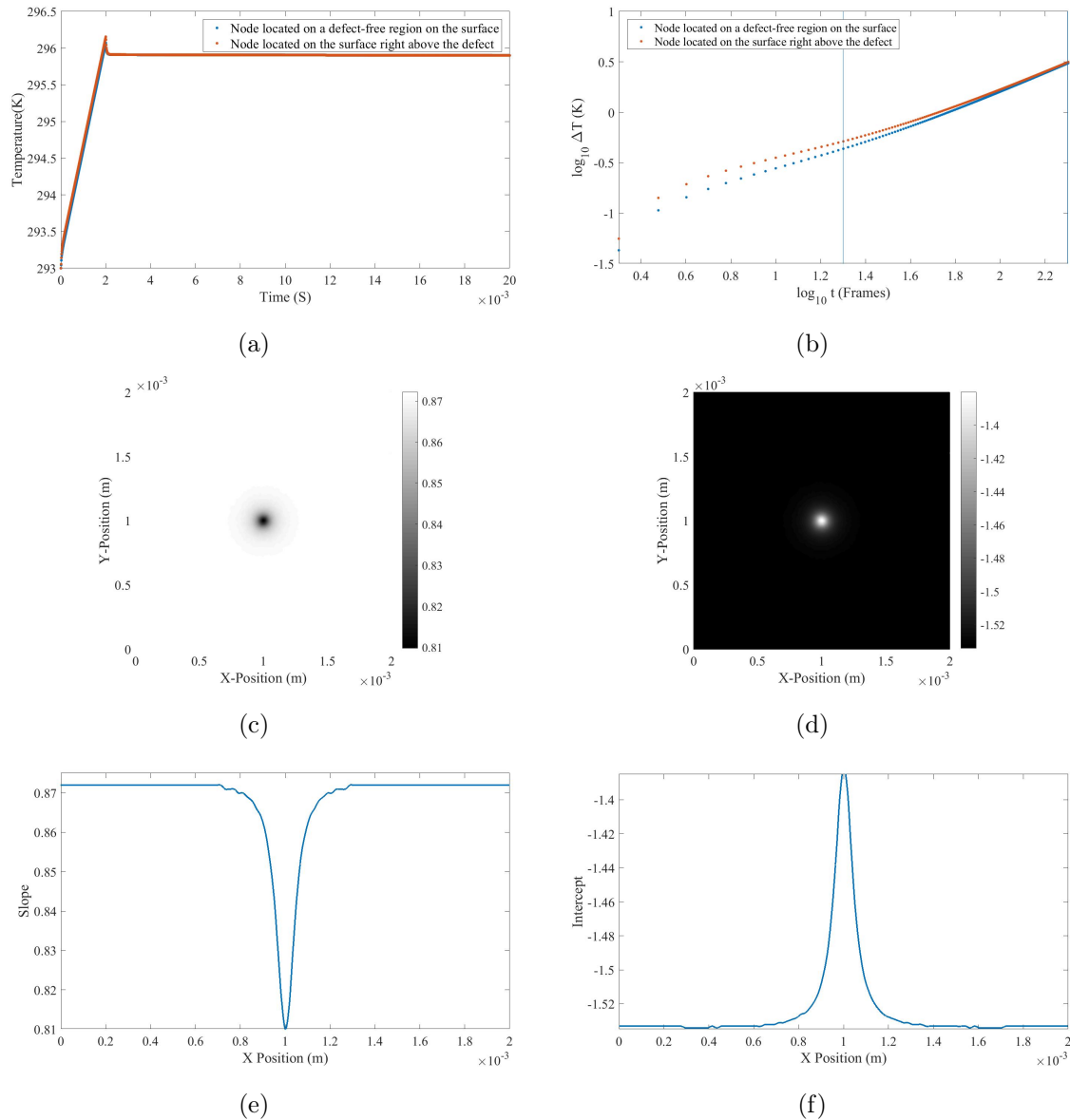


Figure 4.25: (a) Temporal variation of temperature for a 10 μm deep defect in copper. (b) Change in temperature transformed to logarithmic scale.

The defect is shifted to 50 μm and 100 μm from the surface to analyze the defect map and the magnitude of the slope. The c -maps for 50 μm (figure 4.26 (a)) and 100 μm (figure 4.26 (c)) have meager resolution making it difficult to judge the subsurface defect in copper. To increase the resolution, the time step needs to be further decreased to the nano scale, but that is not practical. The frequency of the camera taking the images of the heat diffusion process has to be of the order magnitude of

the Giga scale to capture the signal for this sort of defect in copper. It is possible numerically but not practically.

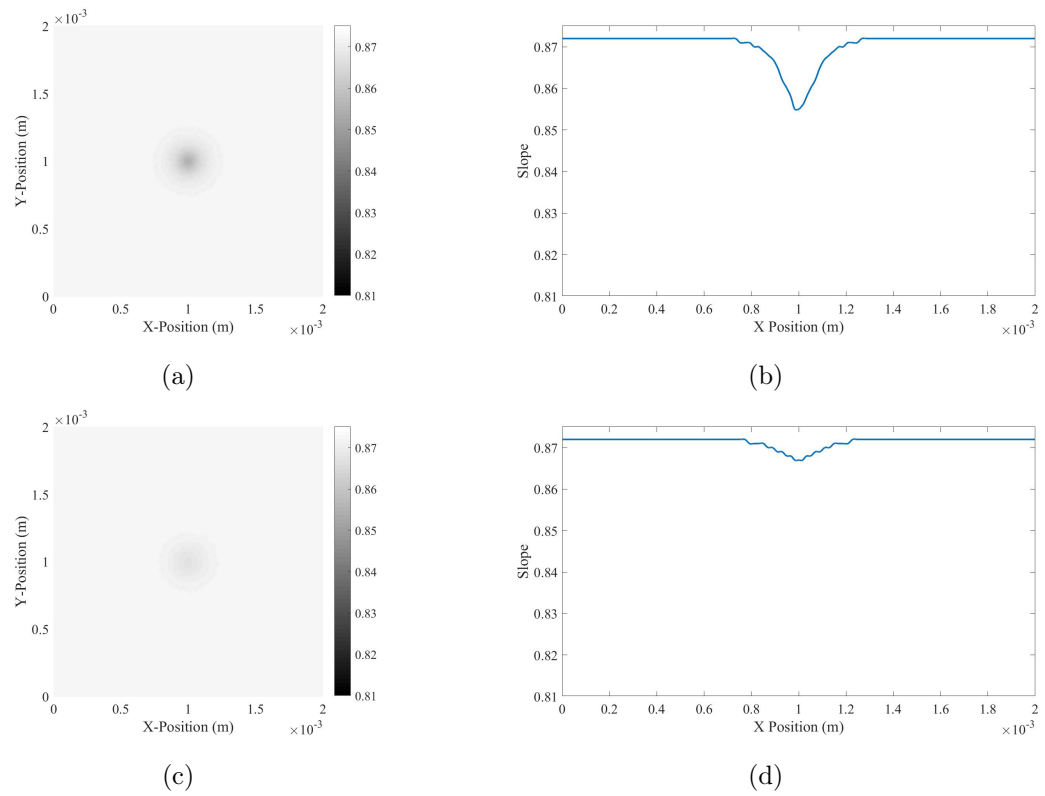


Figure 4.26: For 50 μm deep defect in copper (a) *c*-map. (b) magnitude of slope. For 100 μm deep defect in copper (c) *c*-map. (d) magnitude of slope.

CHAPTER 5: CONCLUSIONS AND FUTURE WORK

5.1 Conclusions

The TSR technique only works when the heat source is well defined. For larger flash durations, the second derivative fails to quantify the defect location because the heat has already been conducted through the defect and analyzing the cooling curve gives a false prediction of the defect. Even if the flash duration is smaller than the diffusion time, the results still depend on the order of the polynomial. It is shown that changing the curve fitting polynomial and skipping post flash data have a huge effect in estimating the depth of the defect. Selection of a higher order polynomial in the curve fitting of the experimental data bears the risk of considering the noise in the approximation of the polynomials.

The CM signal processing technique is successful in addressing the near surface defects and it also takes into account the fact that the heat sources are not always well defined. It uses a first order polynomial for curve fitting, hence it is computationally cheap. The numerical results shows that for multiple defects, the defect needs to be located at a certain distance from each other or else it is difficult to characterize them. The distance of separation depends on the size and shape of the defect. The slope and intercept changes with the change in the depth of the defect. Materials with lower thermal conductivity have a larger diffusion time compared to materials with higher thermal conductivity. The high thermal conductivity of copper makes it difficult to capture the defect for such a thin plate. The material needs to be thick and the defect has to be far from the surface. In order to capture near surface defects in copper, the frame rate of the IR camera needs to be extremely high. The heating curves also provide information regarding the presence of a defect when the diffusion

time is shorter than the flash duration.

5.2 Future Work

The scope of this work can be extended to predict the shape, size and depth of a defect by utilizing defect maps. FEA can be applied to detect different types of defects like cracks, material inclusion, overhang defects, key-hole defects, unfused powder in the bulk, analyzing more complex geometries and adding surface features like surface roughness. Moreover, FT testing of high thermal conducting materials like copper can be used to study the effect of thermal conductivity in assessing the near-surface defect.

REFERENCES

- [1] E. Klar and P. K. Samal, *Powder metallurgy stainless steels: processing, microstructures, and properties*. ASM international, 2007.
- [2] N. Guo and M. C. Leu, “Additive manufacturing: technology, applications and research needs,” *Frontiers of Mechanical Engineering*, vol. 8, pp. 215–243, Sep 2013.
- [3] N. N. Kumbhar and A. V. Mulay, “Post processing methods used to improve surface finish of products which are manufactured by additive manufacturing technologies: A review,” *Journal of The Institution of Engineers (India): Series C*, vol. 99, pp. 481–487, Aug 2018.
- [4] F. Calignano, D. Manfredi, E. P. Ambrosio, S. Biamino, M. Lombardi, E. Atzeni, A. Salmi, P. Minetola, L. Iuliano, and P. Fino, “Overview on additive manufacturing technologies,” *Proceedings of the IEEE*, vol. 105, no. 4, pp. 593–612, 2017.
- [5] A. Lopez, R. Bacelar, I. Pires, T. G. Santos, J. P. Sousa, and L. Quintino, “Non-destructive testing application of radiography and ultrasound for wire and arc additive manufacturing,” *Additive Manufacturing*, vol. 21, pp. 298–306, 2018.
- [6] S. M. Shepard, “Flash thermography of aerospace composites,” in *IV Conferencia Panamericana de END Buenos Aires*, vol. 7, 2007.
- [7] B. Zhang, M. Duemmler, L. Sripragash, O. Adewumi, A. Davies, J. Ziegert, C. Waters, and C. Evans, “Detection of subsurface defect for metal additive manufacturing using flash thermography,” 07 2018.
- [8] R. Usamentiaga, P. Venegas, J. Guerediaga, L. Vega, J. Molleda, and F. Bulnes, “Infrared thermography for temperature measurement and non-destructive testing,” *Sensors*, vol. 14, no. 7, pp. 12305–12348, 2014.
- [9] X. Maldague and S. Marinetti, “Pulse phase infrared thermography,” *Journal of applied physics*, vol. 79, no. 5, pp. 2694–2698, 1996.
- [10] C. Ibarra-Castanedo and X. Maldague, “Pulsed phase thermography reviewed,” *Quantitative Infrared Thermography Journal*, vol. 1, no. 1, pp. 47–70, 2004.
- [11] X. Maldague *et al.*, “Theory and practice of infrared technology for nondestructive testing,” 2001.
- [12] A. A. Badghaish and D. C. Fleming, “Non-destructive inspection of composites using step heating thermography,” *Journal of composite materials*, vol. 42, no. 13, pp. 1337–1357, 2008.
- [13] R. Mulaveesala and S. Tuli, “Theory of frequency modulated thermal wave imaging for nondestructive subsurface defect detection,” *Applied Physics Letters*, vol. 89, no. 19, p. 191913, 2006.

- [14] N. Tabatabaei and A. Mandelis, “Thermal-wave radar: A novel subsurface imaging modality with extended depth-resolution dynamic range,” *Review of Scientific Instruments*, vol. 80, no. 3, p. 034902, 2009.
- [15] Y. He, B. Gao, A. Sophian, and R. Yang, “Chapter 5 - active thermography and eddy current excited thermography,” in *Transient Electromagnetic-Thermal Nondestructive Testing* (Y. He, B. Gao, A. Sophian, and R. Yang, eds.), pp. 93 – 121, Butterworth-Heinemann, 2017.
- [16] S. M. Shepard, “System for generating thermographic images using thermographic signal reconstruction,” May 25 2010. US Patent 7,724,925.
- [17] C. Ibarra-Castanedo, M. Genest, J.-M. Piau, S. Guibert, A. Bendada, and X. P V Maldague, “Chapter x active infrared thermography techniques for the nondestructive testing of materials,” 05 2007.
- [18] B. A. R. D. W. T. A. Steven M. Shepard, James R. Lhota, “Reconstruction and enhancement of active thermographic image sequences,” *Optical Engineering*, vol. 42, no. 5, pp. 1337 – 1342 – 6, 2003.
- [19] S. M. Shepard, “Advances in pulsed thermography,” vol. 4360, 2001.
- [20] M. F. B. Steven M. Shepard, “Advances in thermographic signal reconstruction,” vol. 9485, 2015.
- [21] B. Oswald-Tranta, R. Schmidt, and T. Grandl, “Comparison of samples with flat bottom holes and with hidden occlusions using flash thermography,”
- [22] C. Maierhofer, N. Rothbart, M. Goldammer, F. Hohlstein, J. Koch, I. Kryukov, G. Mahler, B. Stotter, G. Walle, B. Oswald-Tranta¹⁰, *et al.*, “A round robin test of flash thermography—detectability and quantification of artificial and natural defects in cfrp and metal structures,” *Stainless steel*, vol. 1, pp. X5CrNi18–10, 2016.
- [23] T. S. Hunnewell, K. L. Walton, S. Sharma, T. K. Ghosh, R. V. Tompson, D. S. Viswanath, and S. K. Loyalka, “Total hemispherical emissivity of ss 316l with simulated very high temperature reactor surface conditions,” *Nuclear Technology*, vol. 198, no. 3, pp. 293–305, 2017.